

# Kinetic Significance of Proton–Electron Transfer during Condensed Phase Reduction of Carbonyls on Transition Metal Clusters

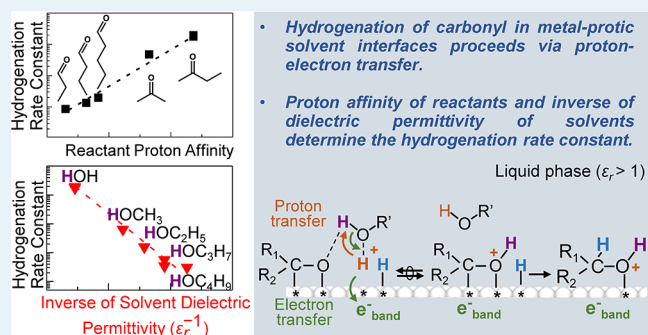
Junnan Shangguan and Ya-Huei Cathy Chin\*<sup>1</sup>

Department of Chemical Engineering and Applied Chemistry, University of Toronto, Toronto, Ontario M5S 3E5, Canada

## Supporting Information

**ABSTRACT:** Kinetic measurements, competitive hydrogenation, and H–D kinetic isotopic studies confirm the prevalence of proton–electron transfer events during the catalytic reduction of aliphatic carbonyls (C<sub>3</sub>–C<sub>6</sub>) at protic solvent and transition-metal (Ru, Pt, and Pd) interfaces. Polar protic solvents assist with the initial, rapid H-atom ionization, which forms a proton and an electron pair. The proton shuffles through the solvent matrix and attacks the carbonyl oxygen in a quasi-equilibrated step, resulting in the formation of a charged hydroxy intermediate as the most abundant reactive intermediate. Subsequently, this intermediate undergoes a kinetically relevant H-atom addition on the carbon atom that forms the charged alcohol, which then recombines with the electron and desorbs as the alcohol product. As a direct consequence of the initial, quasi-equilibrated proton transfer, the first-order rate coefficient increases exponentially as the gas-phase proton affinity of the carbonyls increases or as the inverse of solvent dielectric permittivity ( $\epsilon_r^{-1}$ ) decreases. The initial, quasi-equilibrated proton transfer step onto the carbonyl oxygen, rather than the H-atom transfer to the carbonyl carbon, is consistent with the inverse H<sub>2</sub>–D<sub>2</sub> kinetic isotope effects and with the insignificant H–D exchange on the carbonyl carbon of the reactants. A Born–Haber thermochemical construct captures the free energies of the charged hydroxy intermediates, the most abundant reactive intermediates, and connects the stability of these intermediates with (1) the increase in the reactant proton affinity and (2) the decrease in the inverse of solvent dielectric permittivity, and in turn with higher hydrogenation rates.

**KEYWORDS:** carbonyl compound, hydrogenation, proton affinity, proton–electron transfer, solvent effects, transition-metal clusters



## 1. INTRODUCTION

Catalytic hydrogenation involves sequential additions of hydrogen atoms onto unsaturated C=O, C=C, or C=N functional groups on transition-metal surfaces. These events are ubiquitous and can occur at the interfacial regions of both gas–transition metal surfaces and liquid–transition metal surfaces. Depending on the interface, the specific molecular details of these hydrogen addition events may differ, because the identity and reactivity of the surface hydrogen intermediates depend sensitively on the local environment. At the gas–metal interface, hydrogen adatoms (H-adatoms) derived from H<sub>2</sub> dissociative adsorption on transition-metal surfaces are the reactive intermediates during hydrogenation.<sup>1</sup> For the contrasting case of protic solvent–metal interface, H-adatoms transfer their electrons into the d band of the transition metal and acquire proton character.<sup>2</sup> This ionization event is mechanistically analogous to what occurs during the electrochemical oxidation of hydrogen,<sup>3</sup> also known as the Volmer reaction, on Ni, Pd, Pt, and Ru polycrystalline electrodes.<sup>4</sup> High-resolution electron energy loss spectroscopy (HREELS) on Pt(111)<sup>5a</sup> and low-energy sputtering mass spectroscopy (LES-MS) on Pt(111)<sup>5b</sup> detect the solvated proton (H<sup>+</sup>(H<sub>2</sub>O)<sub>m</sub>, m ≥ 1) formation from the surface reaction between coadsorbed H-atom and H<sub>2</sub>O. The hydrogen ionization is thermodynamically favorable on

Pt(111),<sup>7</sup> Cu(110),<sup>7</sup> Ru(0001),<sup>2a</sup> Ag(111),<sup>8</sup> Au(111),<sup>6</sup> and Pt<sub>66</sub>Ru<sub>33</sub>(111) alloy surfaces,<sup>9</sup> as confirmed from density functional theory (DFT) calculations.

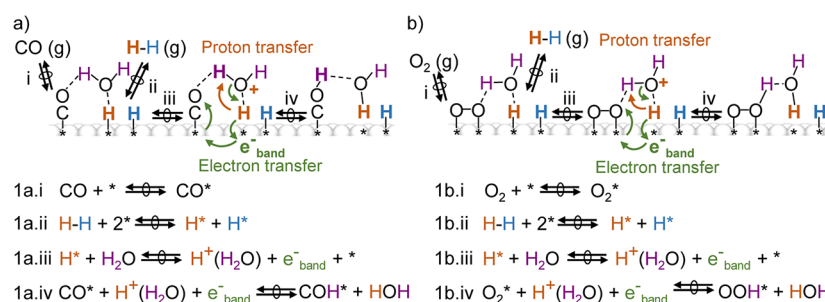
Protons, when they are solvated in a polar protic solvent (e.g., H<sup>+</sup>(H<sub>2</sub>O)<sub>m</sub>, m ≥ 1, in H<sub>2</sub>O solvent), may migrate and transport across the solvent molecular network through rapid hydrogen bond shuffling.<sup>10</sup> Concomitant with this proton shuffling, the electrons formed from the hydrogen ionization must also transfer, but through the d band of the metals in order to maintain the overall charge neutrality of the hydrogen transfer event. The result of these proton–electron transfer (PET) events<sup>11</sup> is the net migration of an H atom via a reaction path mechanistically different from the direct addition of H-atom path typically encountered at the gas–metal interface (without protic molecules). Scheme 1 shows several PET events, previously established in heterogeneous catalytic systems in the presence of vicinal protic molecule(s), of (a) H-addition onto CO during Fischer–Tropsch synthesis on Ru clusters<sup>2a</sup> and (b) H-addition onto O<sub>2</sub> during H<sub>2</sub>O<sub>2</sub> production on Pd clusters.<sup>2b</sup> In both systems, oxygen-containing species (Scheme

Received: August 30, 2018

Revised: December 31, 2018

Published: January 31, 2019

**Scheme 1. H-Atom Ionization and Proton–Electron Transfer (PET) Events during (a) H Addition to CO during Fischer–Tropsch Synthesis on Ru Surfaces<sup>2a</sup> and (b) H Addition to O<sub>2</sub> during H<sub>2</sub>O<sub>2</sub> Production on Pd Surfaces<sup>2b</sup>**



1a, CO; Scheme 1b, O<sub>2</sub>) chemisorb on transition-metal surfaces (steps 1a.i and 1b.i) and H<sub>2</sub> dissociates into H-adatoms (steps 1a.ii and 1b.ii). Subsequently, a protic molecule assists the H-ionization step (steps 1a.iii and 1b.iii) followed by a sequential PET event (steps 1a.iv and 1b.iv), during which protons transfer through the solvent molecule network and electrons transfer from the metal's d band. DFT calculations have established the involvement of protons, derived from surface H\* ionization when it is surrounded by a single H<sub>2</sub>O molecule, in a proton attack to the oxygen of CO\* on Ru<sub>201</sub> clusters as an initiation step in Fischer–Tropsch synthesis at gas–Ru interfaces (Scheme 1a).<sup>2a</sup> In a separate study, kinetic analyses have demonstrated that a similar proton addition mechanism occurs, during which the proton attacks one of the oxygen atoms in O<sub>2</sub>\* on Pd clusters as a route to selective peroxide formation at protic solvent (H<sub>2</sub>O or CH<sub>3</sub>OH)–Pd interfaces (Scheme 1b).<sup>2b</sup>

For the reduction of carbonyl compounds, literature reports have long speculated on the involvement and significance of proton (and electron) transfer during C=O bond hydrogenation, due to the strong rate dependences on solvent identity.<sup>12</sup> In comparison to the hydrogenation rates measured in water, a protic solvent with high dielectric permittivity, the 2-butanone hydrogenation rates decrease by more than 2 orders of magnitude in tetrahydrofuran, an aprotic solvent,<sup>12b</sup> or by 1 order of magnitude in isopropyl alcohol, a protic solvent with dielectric permittivity lower than that of water.<sup>12a</sup> Despite these salient catalytic manifestations and mechanistic speculations,<sup>12a,b</sup> the exact catalytic involvement of proton (and electron) transfer, the link between the PET event and the identity effects of reactant and solvent, and a generalized framework that captures the thermodynamic driving forces for these PET events have remained largely missing. Here, we examine the hydrogenation of carbonyl compounds at the interfaces of a transition-metal cluster (Ru, Pt, Pd) and protic solvent with kinetic and isotopic techniques and derive from this a mechanistic framework that captures the catalytic effects of reactant chemical identity, solvent molecules, and metal identity. Our findings provide rigorous experimental evidence that is consistent with the density functional theory prediction.<sup>12a</sup> Specifically, the rates of C–H/C–D isotopic exchange during *n*-C<sub>3</sub>H<sub>7</sub>C(O)H–D<sub>2</sub> reactions and effective kinetic isotope effects of *n*-C<sub>3</sub>H<sub>7</sub>C(O)H–H<sub>2</sub> and *n*-C<sub>3</sub>H<sub>7</sub>C(O)H–D<sub>2</sub> reactions rule out the direct H-adatom addition route and confirm the prevalence of the PET mechanism, which involves rapid, quasi-equilibrated proton–electron formation and initial proton transfer onto the carbonyl oxygen atom, before the sequential, kinetically relevant H-addition to the carbonyl carbon atom. The quasi-equilibrated proton formation and addition lead to the formation of a charged hydroxy intermediate with an ionic O–H<sup>+</sup> bond. This

charged hydroxy intermediate becomes more stable as the proton affinity of carbonyl compounds increases, as it strengthens the ionic O–H bond, or as the inverse dielectric permittivity of the solvent decreases, as it stabilizes the charged surface intermediate to a larger extent, thus increasing the hydrogenation rates. A generalized Born–Haber thermochemical cycle construct captures these reactivity trends for the various carbonyls and solvents, with the gas-phase proton affinity of carbonyls and dielectric permittivity of solvents as the kinetic descriptors.

## 2. CATALYST SYNTHESIS AND EXPERIMENTAL METHODS

### 2.1. Synthesis of Nanometer-Sized Ru, Pd, and Pt Clusters Dispersed on Porous SiO<sub>2</sub> Particles.

Catalysts with 1 wt % Ru, Pt, and Pd clusters supported on SiO<sub>2</sub> were prepared by incipient wetness impregnation of SiO<sub>2</sub> (Grace, 330 m<sup>2</sup> g<sup>-1</sup>, 1.15 cm<sup>3</sup> g<sup>-1</sup> pore volume, 0–75 μm particle size) with an aqueous precursor solution of Ru(NO)(NO<sub>3</sub>)<sub>3</sub>, Pt(NH<sub>3</sub>)<sub>4</sub>(NO<sub>3</sub>)<sub>3</sub>, and Pd(NO<sub>3</sub>)<sub>3</sub>, respectively (Sigma-Aldrich, CAS and Lot numbers of 34513-98-9 and MKBS7427 V (1.4% Ru), 20634-12-2 and MKBX6144 V (99.995% trace metal basis of Pt), and 207596-32-5 and BCBL5001 V (40% Pd), respectively). The impregnated Ru and Pt samples were treated in ambient air at 348 K for 24 h and then under flowing 5% H<sub>2</sub>/He (0.33 cm<sup>3</sup> g<sup>-1</sup> s<sup>-1</sup>, Linde certified) at 0.03 K s<sup>-1</sup> to 623 K, and then held at 623 K for 6 h for Ru and 5 h for Pt, respectively. The impregnated Pd sample was treated in ambient air at 348 K for 24 h, treated in dry air (Linde, 99.99%, 0.33 cm<sup>3</sup> g<sup>-1</sup> s<sup>-1</sup>) at 0.05 K s<sup>-1</sup> to 673 K, and then held at 673 K for 5 h, before cooling to ambient temperature. This Pd sample was then treated in 5% H<sub>2</sub>/He (0.33 cm<sup>3</sup> g<sup>-1</sup> s<sup>-1</sup>, Linde certified) at 0.03 K s<sup>-1</sup> to 673 K and then held at 673 K for 1 h.

The average Ru and Pt cluster diameter and dispersion were determined from chemisorbed hydrogen uptakes, measured using a volumetric adsorption–desorption apparatus over 0–13 kPa of H<sub>2</sub> at 313 K. The catalysts were first treated in situ under flowing H<sub>2</sub> (Linde certified standard, 99.999%, 0.4 cm<sup>3</sup> g<sup>-1</sup> s<sup>-1</sup>), by heating at 0.03 K s<sup>-1</sup> from ambient temperature to 573 K, holding isothermally at 573 K for 1 h, then exposing to the dynamic vacuum (<5 × 10<sup>-2</sup> Pa) for 12 h at 573 K, and finally cooling to 313 K (~0.08 K s<sup>-1</sup>) for the H<sub>2</sub> uptake measurements. Two sets of H<sub>2</sub> uptakes were carried out isothermally at 313 K, and between each set of the uptake measurements, the catalyst was exposed to dynamic vacuum (<5 × 10<sup>-2</sup> Pa) for 0.5 h. The amount of chemisorbed hydrogen was determined by the difference in H to M (M = Ru, Pt) ratios between the two H<sub>2</sub> uptake values at zero pressure, obtained by extrapolating the H to M ratios at higher pressures, when H to M ratios remained

nearly constant with respect to H<sub>2</sub> pressure, to zero pressure. This value was used to estimate the Ru and Pt dispersion by assuming an H to surface metal atomic ratio of unity. The mean Ru and Pt cluster diameters were estimated from Ru and Pt dispersions, respectively, by assuming a spherical structure with an atomic density identical with Ru bulk and Pt bulk of 13.65 × 10<sup>-3</sup> and 15.10 × 10<sup>-3</sup> nm<sup>3</sup>,<sup>13</sup> respectively.

The Pd dispersion was determined by volumetric O<sub>2</sub> chemisorption at 313 K, after in situ H<sub>2</sub> treatment (Linde certified standard, 99.999%, 0.3 cm<sup>3</sup> g<sup>-1</sup> s<sup>-1</sup>) at 673 K for 1 h, then exposing to the dynamic vacuum (<5 × 10<sup>-2</sup> Pa) for 10 h at 673 K, and finally cooling to 313 K (~0.08 K s<sup>-1</sup>). The metal dispersion of Pd was estimated from the volumetric adsorption isotherms, similar to the method described above for Ru and Pt, by assuming an O to surface metal atomic ratio of unity. The mean Pd cluster diameter was estimated from Pd dispersion, by assuming a spherical structure with an atomic density identical with Pd bulk of 14.70 × 10<sup>-3</sup> nm<sup>3</sup>.<sup>13</sup>

**2.2. Rate Assessments with an Isothermal, Gradientless, Batch-Stirred Tank Reactor.** Initial hydrogenation rates of carbonyl compounds (2-butanone, 99.0%; acetone, 99.5%; pentanal, 97.0%; butanal, 99.0%; propanal, 97.0%; all from Sigma-Aldrich, CAS numbers 78-93-3, 67-64-1, 110-62-3, 123-72-8, and 123-38-6, respectively) were measured in an isothermal batch-stirred tank reactor (300 cm<sup>3</sup>, Parr Instruments, Hastelloy). In each experiment, the solvent volume was maintained at 100 cm<sup>3</sup>, whereas the compositions of solvent were varied either by changing the water content (from 0 to 20 wt %) in water–1,4-dioxane mixtures (doubly deionized water, >18 MΩ cm; 1,4-dioxane, 99.0%, Sigma-Aldrich, CAS number 123-91-1) or by directly changing the solvent media to linear alcohols (i.e., methanol, 99.8%, Sigma-Aldrich; ethanol, 99.8%, Commercial Alcohols; 1-propanol, 99.5%, Sigma-Aldrich; 1-butanol, 99.4%, Caledon; CAS numbers 67-56-1, 64-17-5, 71-23-8, and 71-36-3, respectively). The carbonyl compound solution (0.04–0.07 M) and 10–100 mg 1 wt % M/SiO<sub>2</sub> (M = Ru, Pt, Pt) were placed in the reactor, followed by purging the reactor void space with He (Linde, 99.999%) for 300 s and then heating to 323 K. After the temperature set point was reached, H<sub>2</sub> (10 bar at 323 K, Linde, 99.999%) was introduced into the reactor and the reaction clock time (*t*), defined as the duration of the reaction, was set to zero (*t* = 0) as soon as the agitation speed was set to 900 rpm. After a constant H<sub>2</sub> pressure and agitation speed was maintained for a specific reaction period (0.5–5 h), the mechanical stirrer was stopped and, at this point, the reaction clock time was ended. A small amount of liquid sample (1 cm<sup>-3</sup>) was withdrawn from the dip tube immersed in the reaction solution, and internal standards (i.e., 2-propanol or 1-propanol, 99.5% Sigma-Aldrich) were introduced prior to the quantification of reactants and products using a gas chromatograph (Agilent 7890 A) equipped with a DB-1 column (30 m × 320 μm × 1 μm) connected to a flame ionization detector (FID). The initial hydrogenation turnover rate of the carbonyl compound R<sub>1</sub>C(O)R<sub>2</sub> (R<sub>1</sub> = C<sub>n</sub>H<sub>2n+1</sub> (*n* = 2–4) and R<sub>2</sub> = H; alternatively, R<sub>1</sub> = CH<sub>3</sub>, C<sub>2</sub>H<sub>5</sub> and R<sub>2</sub> = CH<sub>3</sub>),  $-r_{R_1C(O)R_2,M,l}$  (subscript M = Ru, Pt, Pd; the subscript l denotes the solvent identity, l = R'OH or H<sub>2</sub>O–1,4-dioxane mixture), was computed at <15% conversion of the carbonyl reactant and was based on

$$-r_{R_1C(O)R_2,M,l} = \frac{n_{R_1CH(OH)R_2}(t) - n_{R_1CH(OH)R_2}(0)}{n_{M,surf}} \quad (1a)$$

where  $n_{R_1CH(OH)R_2}(t)$ ,  $n_{R_1CH(OH)R_2}(0)$ , and  $n_{M,surf}$  denote the moles of alcohol produced, as quantified by GC-FID, after reaction clock time *t*, the moles of alcohol produced at reaction clock time zero, and the moles of surface metal atoms, respectively.

Competitive hydrogenation of aldehydes (pentanal, 97.0%; butanal, 99.0%; propanal, 97.0%; benzaldehyde, 99.5%; isobutyraldehyde, 98%; all from Sigma-Aldrich; CAS numbers 110-62-3, 123-72-8, 123-38-6, 100-52-7, and 78-84-2, respectively) and ketones (2-butanone, 99.0%; acetone, 99.5%; 4-methyl-2-pentanone, 98.5%; acetophenone, 99.5%; all from Sigma-Aldrich, CAS numbers 78-93-3, 67-64-1, 108-10-1, and 98-86-2) were measured using the reactor configurations and start-up procedure described above at 10 bar of H<sub>2</sub> and 323 K. In these experiments, the carbonyl compound pairs (i.e., 0.03–0.06 M R<sub>3</sub>C(O)H, R<sub>3</sub> = C<sub>2</sub>H<sub>5</sub>, n-C<sub>3</sub>H<sub>7</sub>, n-C<sub>4</sub>H<sub>9</sub>, Ar and 0.04–0.05 M i-C<sub>3</sub>H<sub>7</sub>C(O)H for aldehydes; 0.03–0.06 M R<sub>b</sub>C(O)CH<sub>3</sub>, R<sub>b</sub> = CH<sub>3</sub>, C<sub>2</sub>H<sub>5</sub>, Ar and 0.04–0.05 M i-C<sub>3</sub>H<sub>7</sub>C(O)CH<sub>3</sub> for ketones) and 1 wt % Ru/SiO<sub>2</sub> (10–50 mg) were placed in the reactor. During the reactions, liquid aliquots (~1 cm<sup>3</sup>) were withdrawn periodically (0.5–5 h) for chemical quantifications. After each liquid sampling, the reactor was recharged to 10 bar of H<sub>2</sub> in order to maintain its isobaric condition at 323 K. Internal standards (i.e., 2-propanol or 1-propanol, 99.5% Sigma-Aldrich) were incorporated into the liquid aliquots before the quantification of reactants and products using a gas chromatograph (Agilent 7890 A) equipped with a DB-1 column (30 m × 320 μm × 1 μm) connecting to a flame ionization detector (FID).

**2.3. Time-Dependent Butanal–H<sub>2</sub>–H<sub>2</sub>O and Butanal–D<sub>2</sub>–D<sub>2</sub>O Reactions in an Isothermal, Gradientless, Batch-Stirred Tank Reactor.** Butanal (n-C<sub>3</sub>H<sub>7</sub>C(O)H)–H<sub>2</sub>–H<sub>2</sub>O and n-C<sub>3</sub>H<sub>7</sub>C(O)H–D<sub>2</sub>–D<sub>2</sub>O reactions (95.1% D<sub>2</sub>/N<sub>2</sub>, BOC certified standard; 100 cm<sup>3</sup> D<sub>2</sub>O, 99.9 atom % D, Sigma-Aldrich, CAS number 7789-20-0) were measured with the reactor configurations and start-up procedure described above at 1.3 bar of H<sub>2</sub> or D<sub>2</sub> and 323 K, except that the liquid (~1 cm<sup>3</sup>) was sampled periodically (0.25–1 h) at 323 K. The reactor was recharged to 1.3 bar of H<sub>2</sub> or D<sub>2</sub> after each liquid sampling to maintain its isobaric condition. The n-C<sub>3</sub>H<sub>7</sub>C(O)H–D<sub>2</sub>–D<sub>2</sub>O reactions form n-C<sub>3</sub>H<sub>7</sub>C(O)D and n-C<sub>3</sub>H<sub>7</sub>CHDOD. The deuterium content in butanal (as mixtures of exchange product n-C<sub>3</sub>H<sub>7</sub>C(O)D and original n-C<sub>3</sub>H<sub>7</sub>C(O)H) and 1-butanol (as the hydrogenation product of C<sub>3</sub>H<sub>7</sub>CHDOD) was quantified using a gas chromatograph (Agilent 7890 A)–mass spectrometer (Agilent 5975C, GC-MS), equipped with an HP-5 capillary column (Agilent, 19091J-413, 30 m × 320 μm × 0.25 μm) connected to a mass selective detector. The total amount of butanal and 1-butanol was also quantified by a secondary method in addition to mass selective detection, by first introducing an internal standard (i.e., 2-propanol, 99.5% Sigma-Aldrich) before analyzing with a gas chromatograph (Agilent 7890 A) equipped with a DB-1 column (30 m × 320 μm × 1 μm) connected to a flame ionization detector (FID).

### 3. RESULTS AND DISCUSSION

**3.1. Reactant and Solvent Identity Effects on First-Order Hydrogenation Rate Coefficients and Lumped Hydrogenation Rate Constants during Hydrogenation of Carbonyls at Transition Metal and Protic Solvent Interfaces.** Hydrogenation of C<sub>3</sub>–C<sub>5</sub> carbonyl compounds (R<sub>1</sub>C(O)R<sub>2</sub>, where R<sub>1</sub> = C<sub>n</sub>H<sub>2n+1</sub> (*n* = 2–4) and R<sub>2</sub> = H;

alternatively,  $R_1 = \text{CH}_3$ ,  $\text{C}_2\text{H}_5$  and  $R_2 = \text{CH}_3$ ) on transition-metal clusters (1.8 nm Ru, 1.8 nm Pt, and 2.5 nm Pd, dispersed on  $\text{SiO}_2$ ) forms exclusively the corresponding alcohols ( $\text{R}'\text{C}(\text{OH})\text{R}_2$ , >99.9% selectivity) in pure protic solvents ( $\text{R}'\text{OH}$ ,  $\text{R}' = \text{H}$ ,  $\text{CH}_3$ ,  $\text{C}_2\text{H}_5$ ,  $n\text{-C}_3\text{H}_7$ ,  $n\text{-C}_4\text{H}_9$ ) or in  $\text{H}_2\text{O}$ –1,4-dioxane mixtures (0–25 wt % of  $\text{H}_2\text{O}$ ) at mild hydrogen pressure (10 bar) and 323 K. Since the carbonyl hydrogenation catalysis involves a single carbonyl compound in each of its catalytic sojourns, the initial turnover rate,  $-r_{\text{R}_1\text{C}(\text{O})\text{R}_2, \text{M}, \text{l}}$  (<15% conversion, subscript M = Ru, Pt, Pd; subscript l denotes the solvent identity,  $l = \text{R}'\text{OH}$  or  $\text{H}_2\text{O}$ –1,4-dioxane mixture), is

$$\begin{aligned} -r_{\text{R}_1\text{C}(\text{O})\text{R}_2, \text{M}, \text{l}} &= k_{\text{R}_1\text{C}(\text{O})\text{R}_2, \text{M}, \text{l}}^{\text{1st}} C_{\text{R}_1\text{C}(\text{O})\text{R}_2} \\ &= k_{\text{R}_1\text{C}(\text{O})\text{R}_2, \text{M}, \text{l}}^{\text{lumped}} (\theta_*)^\alpha (P_{\text{H}_2})^\beta C_{\text{R}_1\text{C}(\text{O})\text{R}_2} \end{aligned} \quad (1b)$$

where

$$\begin{aligned} k_{\text{R}_1\text{C}(\text{O})\text{R}_2, \text{M}, \text{l}}^{\text{1st}} &= \frac{-r_{\text{R}_1\text{C}(\text{O})\text{R}_2, \text{M}, \text{l}}}{C_{\text{R}_1\text{C}(\text{O})\text{R}_2}} \\ &= k_{\text{R}_1\text{C}(\text{O})\text{R}_2, \text{M}, \text{l}}^{\text{lumped}} (\theta_*)^\alpha (P_{\text{H}_2})^\beta \end{aligned} \quad (1c)$$

where  $k_{\text{R}_1\text{C}(\text{O})\text{R}_2, \text{M}, \text{l}}^{\text{1st}}$  and  $C_{\text{R}_1\text{C}(\text{O})\text{R}_2}$  denote the first-order rate coefficient and initial concentration of the carbonyl reactant  $\text{R}_1\text{C}(\text{O})\text{R}_2$ , respectively.  $k_{\text{R}_1\text{C}(\text{O})\text{R}_2, \text{M}, \text{l}}^{\text{lumped}}$  denotes the lumped rate constant, which equals the product of equilibrium constants for the various surface elementary events that are required to form the surface precursor (prior to the kinetically relevant step) multiplied by the elementary rate constant of the kinetically relevant step. Thus,  $k_{\text{R}_1\text{C}(\text{O})\text{R}_2, \text{M}, \text{l}}^{\text{lumped}}$  contains the activation free energy between the transition state (in the liquid phase) and reactant state (as  $\text{R}_1\text{C}(\text{O})\text{R}_2(l)$  and  $\text{H}_2(g)$ ).  $\theta_*$  and  $\alpha$  denote the coverage and number of vacant metal sites required to hydrogenate  $\text{R}_1\text{C}(\text{O})\text{R}_2$  at the interface of the transition metal and solvent, respectively.  $P_{\text{H}_2}$  denotes the  $\text{H}_2$  pressure;  $\beta$  denotes the reaction order with respect to  $\text{H}_2$  pressure, and its value reflects the number of H-addition events required for the carbonyl compounds to evolve the transition state. The coverage of vacant metal sites,  $\theta_*$ , is

$$\theta_* = \frac{[*]}{[*] + \sum [z^*]} \quad (1d)$$

where  $[*]$  and  $[z^*]$  denote the surface densities of vacant sites and of all adsorbed intermediates  $z^*$ , which include carbonyl-derived,  $\text{H}_2$ -derived, or solvent-derived species, respectively. The rate expression also accounts for the case in which the coverages of carbonyl-derived intermediates become significant and the apparent reaction order with respect to the carbonyl reactant rate decreases to below unity (eqs 1b–1d).

Defining the function  $f_{\text{R}_1\text{C}(\text{O})\text{R}_2, \text{M}, \text{l}}(\theta_*, P_{\text{H}_2})$ , which captures the influence of vacant metal site and  $\text{H}_2$  pressures, and substituting this term into eq 1c lead to

$$f_{\text{R}_1\text{C}(\text{O})\text{R}_2, \text{M}, \text{l}}(\theta_*, P_{\text{H}_2}) = (\theta_*)^\alpha (P_{\text{H}_2})^\beta \quad (1e)$$

$$k_{\text{R}_1\text{C}(\text{O})\text{R}_2, \text{M}, \text{l}}^{\text{1st}} = k_{\text{R}_1\text{C}(\text{O})\text{R}_2, \text{M}, \text{l}}^{\text{lumped}} f_{\text{R}_1\text{C}(\text{O})\text{R}_2, \text{M}, \text{l}}(\theta_*, P_{\text{H}_2}) \quad (1f)$$

We expect the function  $f_{\text{R}_1\text{C}(\text{O})\text{R}_2, \text{M}, \text{l}}(\theta_*, P_{\text{H}_2})$  to remain identical for the hydrogenation reactions across these carbonyl compounds, because the number of sites in the kinetically relevant step and the number of hydrogen addition events

required to evolve the kinetically relevant transition state remain identical in these reactions. Table 1 summarizes the main symbols defined throughout the discussion and provides their definitions.

**Table 1. Symbols and Their Definitions**

symbol	meaning
$\text{R}_1\text{C}(\text{O})\text{R}_2$	carbonyl reactant ( $R_1 = \text{C}_n\text{H}_{2n+1}$ ( $n = 2-4$ ) and $R_2 = \text{H}$ ; alternatively, $R_1 = \text{CH}_3$ , $\text{C}_2\text{H}_5$ and $R_2 = \text{CH}_3$ )
$r_{\text{R}_1\text{C}(\text{O})\text{R}_2, \text{M}, \text{l}}$	hydrogenation turnover rate (per exposed metal atom) of carbonyl compound on metal surfaces M (M = Ru, Pt, Pd) in the condensed phase l ( $l = \text{R}'\text{OH}$ or $\text{H}_2\text{O}$ –1,4-dioxane mixture)
$k_{\text{R}_1\text{C}(\text{O})\text{R}_2, \text{M}, \text{l}}^{\text{1st}}$	first-order rate coefficient
$k_{\text{R}_1\text{C}(\text{O})\text{R}_2, \text{M}, \text{l}}^{\text{lumped}}$	lumped rate constant
$\theta_*$	fraction of metal sites not occupied by reactive intermediates
$z^*$	adsorbed species z on metal surfaces in the condensed phase
$C_{\text{R}_1\text{C}(\text{O})\text{R}_2}$	concentration of carbonyl reactant
$P_{\text{H}_2}$	$\text{H}_2$ pressure
$f_{\text{R}_1\text{C}(\text{O})\text{R}_2, \text{M}, \text{l}}(\theta_*, P_{\text{H}_2})$	function that captures the rate effects of the vacant metal sites and $\text{H}_2$ pressure
$\epsilon_r$	solvent dielectric permittivity
$PA_{\text{R}_1\text{C}(\text{O})\text{R}_2(g)}$	reactant gas-phase proton affinity
$\Delta G_j$ , $\Delta H_j$ , and $\Delta S_j$	reaction free energy, enthalpy, and entropy of step j
$\text{BDE}_{\text{A}-\text{B}(g)}$	bond dissociation energy of bond A–B in the gas phase
$\Delta G_{\text{sol}, z(g)}$	solvation free energy of gas-phase species z to condensed liquid phase (l)
<i>KIE</i> and <i>EIE</i>	kinetic and equilibrium isotope effects, respectively
<i>ZPE</i>	zero-point energy

Figure 1a shows the effects of the gas-phase reactant proton affinity ( $PA_{\text{R}_1\text{C}(\text{O})\text{R}_2(g)}$ ), defined as the negative heat of reaction for the carbonyl to undergo protonation ( $\text{R}_1\text{C}(\text{O})\text{R}_2 + \text{H}^+ \rightarrow \text{R}_1\text{C}(\text{OH})^+\text{R}_2$ ;  $-PA_{\text{R}_1\text{C}(\text{O})\text{R}_2(g)}$ <sup>14</sup>), also an indication of the thermodynamic tendency for the carbonyl oxygen to accept a proton, on the rate coefficient  $k_{\text{R}_1\text{C}(\text{O})\text{R}_2, \text{M}, \text{H}_2\text{O}}^{\text{1st}}$  during  $\text{R}_1\text{C}(\text{O})\text{R}_2$  hydrogenation on Ru, Pt, and Pd clusters in liquid water at 10 bar of  $\text{H}_2$  and 323 K. The  $k_{\text{R}_1\text{C}(\text{O})\text{R}_2, \text{M}, \text{H}_2\text{O}}^{\text{1st}}$  values increase exponentially with increasing  $PA_{\text{R}_1\text{C}(\text{O})\text{R}_2(g)}$ , irrespective of the catalyst metal identity. The exponential dependences between  $k_{\text{R}_1\text{C}(\text{O})\text{R}_2, \text{M}, \text{H}_2\text{O}}^{\text{1st}}$  and  $PA_{\text{R}_1\text{C}(\text{O})\text{R}_2(g)}$  suggest that carbonyl protonation occurs before the kinetically relevant step; the incipient ionization of surface hydrogen adatom ( $\text{H}^*$ ) has been known to occur (analogous to steps 1a.iii and 1b.iii of Scheme 1), which generates a nearly fully formed proton, before its sequential addition onto the carbonyl oxygen atom, as we will confirm next in section 3.2.

Figure 1b shows the effects of solvent on  $k_{\text{C}_2\text{H}_5\text{C}(\text{O})\text{CH}_3, \text{Ru}, \text{l}}^{\text{1st}}$  ( $l = \text{R}'\text{OH}$ ,  $\text{H}_2\text{O}$ –1,4-dioxane mixture) during the hydrogenation of  $\text{C}_2\text{H}_5\text{C}(\text{O})\text{CH}_3$  (0.06 M) on Ru clusters, in either pure protic  $\text{R}'\text{OH}$  solvents or  $\text{H}_2\text{O}$ –1,4-dioxane binary mixtures at 10 bar of  $\text{H}_2$  and 323 K. The solvent dielectric permittivity ( $\epsilon_r$ ) reflects the solvation free energy provided from the dielectric continuum (i.e., the solvent) to the charged solute, as described by the Born equation.<sup>15</sup> In Figure 1b,  $k_{\text{C}_2\text{H}_5\text{C}(\text{O})\text{CH}_3, \text{Ru}, \text{l}}^{\text{1st}}$  decreases exponentially with  $\epsilon_r^{-1}$ , the inverse of solvent dielectric permittivity in both sets of solvent mixtures. The decrease is much more significant in  $\text{H}_2\text{O}$ –1,4-dioxane binary mixtures than pure protic  $\text{R}'\text{OH}$  solvents. Blending 1,4-dioxane with  $\text{H}_2\text{O}$  not only

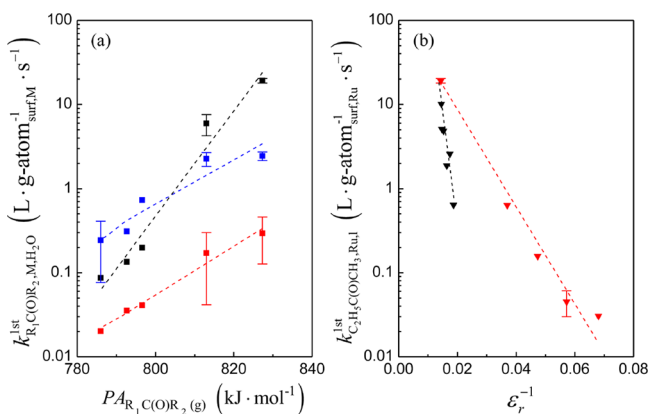


**Figure 1.** (a) First-order rate coefficient,  $k_{R_1C(O)R_2, M, H_2O}^{1st}$  (subscript M = Ru, Pt, Pd), during aqueous-phase hydrogenation of carbonyl compounds (0.04–0.07 M  $C_2H_5C(O)H$ ,  $C_3H_7C(O)H$ ,  $C_4H_9C(O)H$ ,  $CH_3C(O)CH_3$ , and  $C_2H_5C(O)CH_3$ ), plotted as a function of the gas-phase proton affinities of the carbonyl reactants,  $PA_{R_1C(O)R_2(g)}$  on Ru (black ■, 1.8 nm average Ru cluster diameter, 1 wt % Ru/SiO<sub>2</sub>), Pt (blue ■, 1.8 nm average Pt cluster diameter, 1 wt % Pt/SiO<sub>2</sub>), and Pd (red ■, 2.5 nm average Pd cluster diameter, 1 wt % Pd/SiO<sub>2</sub>) clusters at 10 bar of H<sub>2</sub> (charged at 323 K) and 323 K (dotted lines give the best exponential fits with  $R^2$  values of 0.968, 0.886, and 0.980 for Ru, Pt, and Pd, respectively; the error bar indicates the standard deviation of the measurements). (b) First-order rate coefficient,  $k_{C_2H_5C(O)CH_3, Ru, l}^{1st}$  (subscript l denotes the solvent identity, l = R'OH, H<sub>2</sub>O–1,4-dioxane mixture), plotted as a function of inverse solvent dielectric permittivity ( $\epsilon_r^{-1}$ ,  $\epsilon_r$  values obtained from the literature for pure R'OH<sup>30</sup> and calculated on the basis of an empirical equation<sup>31</sup> for H<sub>2</sub>O–1,4-dioxane mixtures) in R'OH (red ▼) or in H<sub>2</sub>O–1,4-dioxane mixtures (black ▼) on Ru clusters (1.8 nm average Ru cluster diameter, 1 wt % Ru/SiO<sub>2</sub>) at 10 bar of H<sub>2</sub> (charged at 323 K) and 323 K (dotted lines are the best exponential fits with  $R^2 = 0.992$  and 0.913 for pure R'OH and H<sub>2</sub>O–1,4-dioxane mixtures, respectively; the error bar indicates the standard deviation of the measurements).

increases the  $\epsilon_r^{-1}$  value but also depletes the concentration of protic H<sub>2</sub>O molecules and that of H<sup>+</sup>(H<sub>2</sub>O)<sub>m</sub> ions ( $m \geq 1$ ). Both factors appear to decrease  $k_{C_2H_5C(O)CH_3, Ru, l}^{1st}$ , an indication that protons may play a significant catalytic role in hydrogenation.

Both the proton affinity of the carbonyl reactant and the dielectric permittivity of solvent are thermodynamic properties independent of the identity and properties of transition-metal surfaces. For this reason, the reactivity trends of these properties on the first-order rate coefficients,  $k_{R_1C(O)R_2, M, l}^{1st}$ , in Figure 1a,b must be a direct result of their influence on the lumped rate constant,  $k_{R_1C(O)R_2, M, l}^{lumped}$ , and not on the term  $f_{R_1C(O)R_2, M, l}(\theta_*, P_{H_2})$  (in eq 1f). This is because the heats of adsorption of carbonyl and solvent-derived intermediates (i.e.,  $z^*$ , eq 1d) do not vary significantly with their carbon chain length; thus, the density of vacant sites and coverages of the various intermediates remain largely independent of carbonyl and solvent identity.

In fact, competitive hydrogenation with two different carbonyl reactants allows the direct assessments of both the first-order rate coefficient ratio and lumped rate constant ratio of the carbonyl reactant pair in identical reaction environments, as this technique ensures that the relative abundance of the various reactive intermediates, surface density of exposed metal sites, and solvation environments remain the same during rate assessments, i.e., the  $f_{R_1C(O)R_2, M, l}(\theta_*, P_{H_2})$  term in the rate equation remains identical for both carbonyls and therefore,

when the rate coefficient ratio of these carbonyls is taken, this term cancels out. Thus, it allows the direct, quantitative measurements of the lumped rate constants. Such strategies have been previously established for the liquid-phase competitive hydrogenation of aromatics on Raney nickel in the liquid phase.<sup>16</sup> We adapt this strategy and confirm the observed, direct effects of proton affinity on the first-order rate coefficients and lumped rate constants, as shown in Figure 1a.

On an Ru cluster (1.8 nm), time-dependent competitive hydrogenation of aldehydes ( $R_aC(O)H$ ) in the  $R_aC(O)H$  and  $i-C_3H_7C(O)H$  reactant mixture in H<sub>2</sub>O (0.03–0.06 M,  $R_a = C_2H_5$ ,  $n-C_3H_7$ ,  $n-C_4H_9$ , Ar, 0.04–0.05 M  $i-C_3H_7C(O)H$ ) at 323 K and 10 bar of H<sub>2</sub> forms  $R_aCH_2OH$  and  $i-C_3H_7CH_2OH$  as the sole products. Under similar conditions, time-dependent competitive hydrogenation of ketones ( $R_bC(O)CH_3$ ) in the  $R_bC(O)CH_3$  and  $i-C_3H_7C(O)CH_3$  reactant mixture in H<sub>2</sub>O at 10 bar H<sub>2</sub> (0.03–0.06 M  $R_bC(O)CH_3$ ,  $R_b = CH_3$ ,  $C_2H_5$ , Ar, 0.04–0.05 M  $i-C_3H_7C(O)CH_3$ ) leads to  $R_bCH_2OH$  and  $i-C_3H_7C(OH)CH_3$ . The rate ratio of  $R_aC(O)H$  to  $i-C_3H_7C(O)H$ ,  $-r_{R_aC(O)H, Ru, H_2O} / -r_{i-C_3H_7C(O)H, Ru, H_2O}$ , derived by substituting eq 1b into the ideal, batch reactor design equation, is

$$\begin{aligned} \frac{-r_{R_aC(O)H, Ru, H_2O}}{-r_{i-C_3H_7C(O)H, Ru, H_2O}} &= \frac{k_{R_aC(O)H, Ru, H_2O}^{1st}}{k_{i-C_3H_7C(O)H, Ru, H_2O}^{1st}} \frac{C_{R_aC(O)H}(t)}{C_{i-C_3H_7C(O)H}(t)} \\ &= \frac{-\frac{d[C_{R_aC(O)H}(t)]}{dt} S_M}{-\frac{d[C_{i-C_3H_7C(O)H}(t)]}{dt} S_M} = \frac{d[C_{R_aC(O)H}(t)]}{d[C_{i-C_3H_7C(O)H}(t)]} \end{aligned} \quad (2)$$

where  $t$  denotes the reaction clock time,  $C_{R_aC(O)H}(t)$  and  $C_{i-C_3H_7C(O)H}(t)$  denote the instantaneous concentration of  $R_aC(O)H$  and  $i-C_3H_7C(O)H$ , respectively, and  $S_M$  denotes the Ru site density per liquid volume. Solving the integral in eq 2 by separation of variables gives

$$\begin{aligned} -\ln \left[ \frac{C_{R_aC(O)H}(t)}{C_{R_aC(O)H}(0)} \right] \\ = - \frac{k_{R_aC(O)H, Ru, H_2O}^{1st}}{k_{i-C_3H_7C(O)H, Ru, H_2O}^{1st}} \ln \left[ \frac{C_{i-C_3H_7C(O)H}(t)}{C_{i-C_3H_7C(O)H}(0)} \right] \end{aligned} \quad (3a)$$

where  $C_{R_aC(O)H}(0)$  and  $C_{i-C_3H_7C(O)H}(0)$  denote the initial concentrations of  $R_aC(O)H$  and  $i-C_3H_7C(O)H$ , respectively. By defining a new parameter  $\omega_{R_1C(O)R_2}(t)$  as

$$\omega_{R_1C(O)R_2}(t) = - \ln \left[ \frac{C_{R_1C(O)R_2}(t)}{C_{R_1C(O)R_2}(0)} \right] \quad (3b)$$

and substituting it into eq 3a, eq 3a becomes

$$\omega_{R_aC(O)H}(t) = \frac{k_{R_aC(O)H, Ru, H_2O}^{1st}}{k_{i-C_3H_7C(O)H, Ru, H_2O}^{1st}} \omega_{i-C_3H_7C(O)H}(t) \quad (3c)$$

Each competitive hydrogenation experiment of the aldehyde pair  $R_aC(O)H$  and  $i-C_3H_7C(O)H$  occurs on metal cluster surfaces at identical coverages and hydrogen pressures. For this reason, the first-order rate coefficient ratio,  $k_{R_aC(O)H, Ru, H_2O}^{1st} / k_{i-C_3H_7C(O)H, Ru, H_2O}^{1st}$ , after expanding each rate coefficient term with eq 1c, becomes

$$\begin{aligned} & \frac{k_{R_aC(O)H,Ru,H_2O}^{1st}}{k_{i-C_3H_7C(O)H,Ru,H_2O}^{1st}} \\ &= \frac{k_{R_aC(O)H,Ru,H_2O}^{lumped} f_{R_aC(O)H,Ru,H_2O}(\theta_*, P_{H_2})}{k_{i-C_3H_7C(O)H,Ru,H_2O}^{lumped} f_{i-C_3H_7C(O)H,Ru,H_2O}(\theta_*, P_{H_2})} \\ &= \frac{k_{R_aC(O)H,Ru,H_2O}^{lumped}}{k_{i-C_3H_7C(O)H,Ru,H_2O}^{lumped}} \end{aligned} \quad (3d)$$

The terms  $f_{R_aC(O)H,Ru,H_2O}(\theta_*, P_{H_2})$  and  $f_{i-C_3H_7C(O)H,Ru,H_2O}(\theta_*, P_{H_2})$  are identical with each other, because the instantaneous site concentration  $\theta_*$  and kinetic dependence on  $P_{H_2}$  remain the same in the competitive reactions. Substituting eq 3d into eq 3c gives

$$\begin{aligned} \omega_{R_aC(O)H}(t) &= \frac{k_{R_aC(O)H,M,H_2O}^{1st}}{k_{i-C_3H_7C(O)H,M,H_2O}^{1st}} \omega_{i-C_3H_7C(O)H}(t) \\ &= \frac{k_{R_aC(O)H,M,H_2O}^{lumped}}{k_{i-C_3H_7C(O)H,M,H_2O}^{lumped}} \omega_{i-C_3H_7C(O)H}(t) \end{aligned} \quad (3e)$$

Similar approaches and derivation for the ketone reactant pair,  $R_bC(O)CH_3$  and  $i-C_3H_7C(O)CH_3$ , lead to

$$\begin{aligned} \omega_{R_bC(O)CH_3}(t) &= \frac{k_{R_bC(O)CH_3,M,H_2O}^{1st}}{k_{i-C_3H_7C(O)CH_3,M,H_2O}^{1st}} \omega_{i-C_3H_7C(O)CH_3}(t) \\ &= \frac{k_{R_bC(O)CH_3,M,H_2O}^{lumped}}{k_{i-C_3H_7C(O)CH_3,M,H_2O}^{lumped}} \omega_{i-C_3H_7C(O)CH_3}(t) \end{aligned} \quad (4)$$

From eqs 3e and 4, the first-order rate coefficient ratios,  $k_{R_aC(O)H,Ru,H_2O}^{1st}/k_{i-C_3H_7C(O)H,Ru,H_2O}^{1st}$  and  $k_{R_bC(O)CH_3,Ru,H_2O}^{1st}/k_{i-C_3H_7C(O)CH_3,Ru,H_2O}^{1st}$  equal their respective lumped rate constant ratios,  $k_{R_aC(O)H,M,H_2O}^{lumped}/k_{i-C_3H_7C(O)H,M,H_2O}^{lumped}$  and  $k_{R_bC(O)CH_3,M,H_2O}^{lumped}/k_{i-C_3H_7C(O)CH_3,M,H_2O}^{lumped}$ . Equation 3e predicts that  $\omega_{R_aC(O)H}(t)$  increases linearly with  $\omega_{i-C_3H_7C(O)H}(t)$ , as confirmed with the data of aliphatic aldehydes ( $R_a = C_2H_5, n-C_3H_7, n-C_4H_9$ ) in Figure 2; this trend extends to and remains similar to that for benzaldehyde ( $R_a = Ar$ , Figure 2d), an aromatic aldehyde with higher gas-phase proton affinity due to the aromaticity (834 kJ mol<sup>-1</sup>)<sup>14</sup> and thus more reactive carbonyl species. Similarly, eq 4 predicts that  $\omega_{R_bC(O)CH_3}(t)$  increases linearly with  $\omega_{i-C_3H_7C(O)CH_3}(t)$ , as also confirmed experimentally with aliphatic ketones ( $R_b = CH_3, C_2H_5$ ) in Figure 3; the trend remains similar, on extension to acetophenone ( $R_b = Ar$ , Figure 3c), an aromatic ketone with higher gas-phase proton affinity due to the aromaticity (861 kJ mol<sup>-1</sup>)<sup>14</sup> and thus more reactive carbonyl species. The slope derived from the linear relation in Figure 2 reflects both the first-order rate coefficient ratio and lumped rate constant ratios for the aldehyde to  $i-C_3H_7C(O)H$ , according to eq 3e. Similarly, the slope of the data in Figure 3 reflects those for the ketone to  $i-C_3H_7C(O)CH_3$  (eq 4).

Figure 4a,b plots  $k_{R_aC(O)H,Ru,H_2O}^{1st}/k_{i-C_3H_7C(O)H,Ru,H_2O}^{1st}$  (also  $k_{R_aC(O)H,M,H_2O}^{lumped}/k_{i-C_3H_7C(O)H,M,H_2O}^{lumped}$ , eq 3e) and  $k_{R_bC(O)CH_3,Ru,H_2O}^{1st}/k_{i-C_3H_7C(O)CH_3,Ru,H_2O}^{1st}$  (also  $k_{R_bC(O)CH_3,M,H_2O}^{lumped}/k_{i-C_3H_7C(O)CH_3,M,H_2O}^{lumped}$ , eq

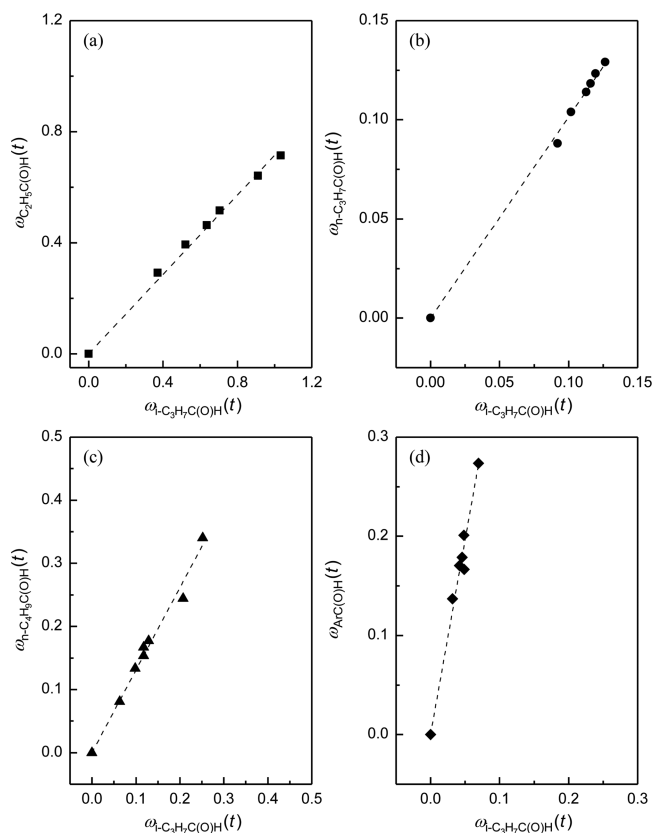


**Figure 2.**  $\omega_{R_aC(O)H}(t)$  (eq 3e) as a function of  $\omega_{i-C_3H_7C(O)H}(t)$  for  $R_a = C_2H_5$  (a),  $n-C_3H_7$  (b),  $n-C_4H_9$  (c), Ar (d), during competitive aldehyde hydrogenation reactions in the aqueous phase (0.03–0.06 M carbonyl compounds) at 10 bar of  $H_2$  and 323 K on 10–100 mg of 1 wt % Ru/SiO<sub>2</sub> (1.8 nm). Dotted lines are the best linear fits with  $R^2$  values of 0.999, 0.999, 0.998, and 0.998 for (a)–(d), respectively.

4) as a function of the gas-phase proton affinity of the  $R_aC(O)H$  and  $R_bC(O)CH_3$  reactants, respectively. These reactivity trends thus reflect the difference in the lumped rate constant (i.e., as  $\Delta(k_{R_aC(O)R_2,M,aq}^{lumped})$ ) among the aliphatic carbonyls. These first-order rate coefficient ratios of aliphatic carbonyls increase exponentially with increasing gas-phase proton affinity of these carbonyl reactants. For aliphatic carbonyls, these trends in rate coefficient ratio from competitive reactions in Figure 4 are consistent with those in Figure 1a, indicating that the reactivity trends in Figure 1 remain uncorrupted by the difference in surface coverages or in site availability. These reactivity trends thus reflect the lumped rate constant differences among the aliphatic carbonyls. The first-order rate coefficient ratio between  $Ar-C(O)CH_3$  (acetophenone) and  $i-C_3H_7C(O)CH_3$  is much higher than the predicted trend among aliphatic ketones (Figure 4b). This deviation may arise from the greater stabilization of the relevant transition state, caused by the presence of an aromatic ring, lowering the activation free energies and leading the lumped rate constant of acetophenone to be higher than that predicted from the general reactivity trends of aliphatic ketones (Figure 4b).

The salient rate dependences on the reactant's proton affinity (Figures 1a and 4) and solvent's dielectric permittivity (Figure 1b) suggest that proton formation and transfer occur before the kinetically relevant step. By inference, pathways that involve only the direct H-atom ( $H^*$ ) addition events, which include the *Alkoxy* pathway, where an  $H^*$  addition first adds to the

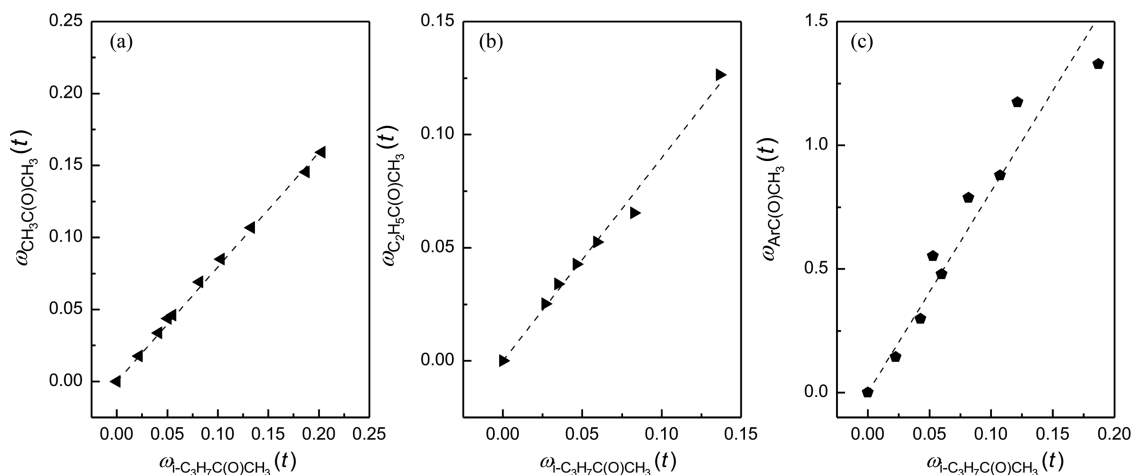


**Figure 3.**  $\omega_{R_bC(O)CH_3}(t)$  (eq 4) as a function of  $\omega_{i-C_3H_7C(O)CH_3}(t)$  for  $R_b = CH_3$  (a),  $C_2H_5$  (b), Ar (c), during competitive ketone hydrogenation reactions in the aqueous phase (0.03–0.06 M carbonyl compounds) at 10 bar of  $H_2$  and 323 K on 10–100 mg of 1 wt % Ru/SiO<sub>2</sub> (1.8 nm). Dotted lines are the best linear fits of eq 4 with  $R^2$  values of 0.999, 0.998, and 0.990 for (a)–(c), respectively.

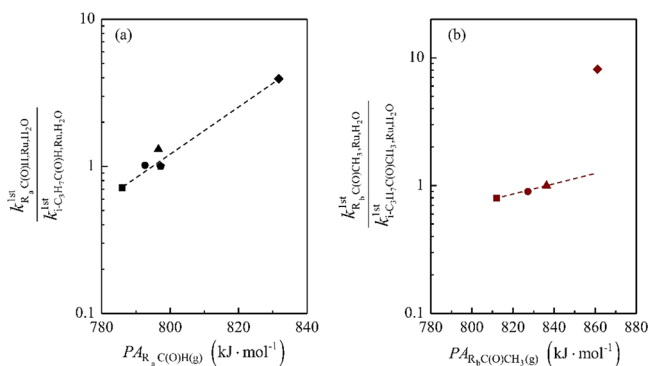


**Figure 4.** (a) First-order rate coefficient ratios of  $R_bC(O)H$  ( $R_b = C_2H_5$  (black ■),  $n-C_3H_7$  (black ●),  $i-C_3H_7$  (black ◆),  $n-C_4H_9$  (black ▲), Ar (black ◆)) to  $i-C_3H_7C(O)H$ ,  $k_{R_bC(O)H,Ru,H_2O}^{1st}/k_{i-C_3H_7C(O)H,Ru,H_2O}^{1st}$  (equivalent to  $k_{R_bC(O)H,Ru,H_2O}^{lumped}/k_{i-C_3H_7C(O)H,Ru,H_2O}^{lumped}$ , eq 3e), extrapolated from linear regression of the data in Figure 2 against eq 3e as the objective function, plotted as a function of their gas-phase proton affinity ( $PA_{R_bC(O)H(g)}$ ) (the dotted line gives the best exponential fit,  $R^2 = 0.971$ ). (b) First-order rate coefficient ratios of  $R_bC(O)CH_3$  ( $R_b = CH_3$  (brown ■),  $C_2H_5$  (brown ●),  $i-C_3H_7$  (brown ▲), or Ar (brown ◆)) to  $i-C_3H_7C(O)CH_3$ ,  $k_{R_bC(O)CH_3,Ru,H_2O}^{1st}/k_{i-C_3H_7C(O)CH_3,Ru,H_2O}^{1st}$  (equivalent to  $k_{R_bC(O)CH_3,Ru,H_2O}^{lumped}/k_{i-C_3H_7C(O)CH_3,Ru,H_2O}^{lumped}$ , eq 4), extrapolated from the linear regression of Figure 3 by using eq 4 as the objective function, plotted as a function of their gas-phase proton affinity ( $PA_{R_bC(O)CH_3(g)}$ ) (the dotted line gives the best exponential fit,  $R^2 = 0.986$ ).

carbonyl carbon and a second  $H^*$  adds to the oxygen of the carbonyl function,<sup>1a,12a,17</sup> or the alternate *Hydroxy* pathway, where the sequence of  $H^*$  additions is reversed, remain kinetically irrelevant.

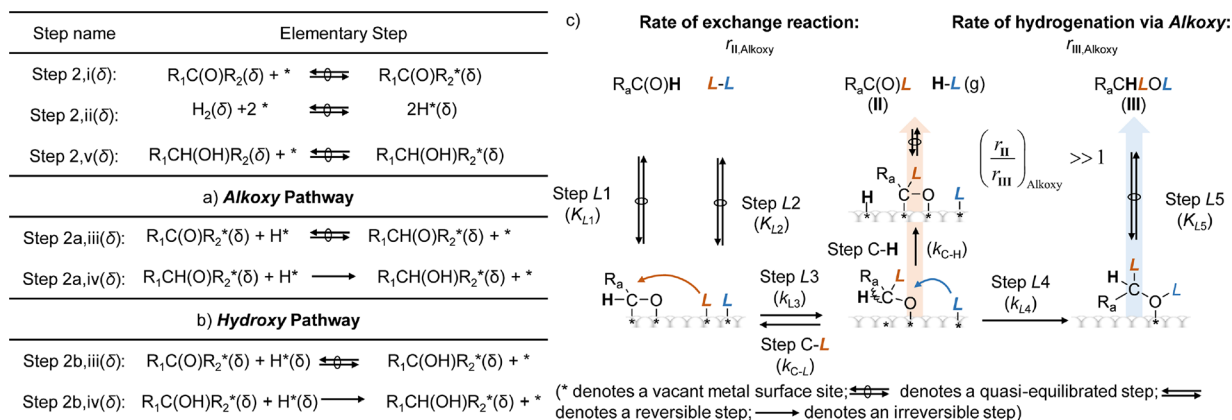
**3.2. Deciphering the Catalytic Pathways with H–D Exchange Studies and Kinetic Isotope Effect Measurements with Butanal–D<sub>2</sub>–D<sub>2</sub>O Mixtures on Ru Clusters.** In this section, we rule out the kinetic prevalence of pathways that involve solely the addition of  $H^*$ . There are two plausible pathways, depending on the sequence of the H-addition steps: (i) the *Alkoxy* pathway, where an  $H^*$  first attacks the carbonyl carbon before a second  $H^*$  attacks the oxygen, and (ii) the *Hydroxy* pathway, where the  $H^*$  addition sequence is reversed, i.e., first  $H^*$  added to the oxygen before the second  $H^*$  addition

to carbonyl carbon. The former *Alkoxy* pathway was proposed on the basis of DFT calculations as the pathway with the lowest overall activation enthalpy for the hydrogenation of C<sub>1</sub>–C<sub>4</sub> aliphatic carbonyl compounds on a vacuum–Ru(0001) interface<sup>1a</sup> and on rate dependences for C<sub>3</sub>–C<sub>5</sub> ketone reactions at the vapor–Ru interface;<sup>17b</sup> the latter *Hydroxy* pathway was examined as the competing pathway and was shown to occur much more slowly than the *Alkoxy* pathway for the case of C<sub>1</sub>–C<sub>4</sub> aliphatic carbonyl compounds on a vacuum–Ru(0001) interface.<sup>1a</sup> We consider both *Alkoxy* and *Hydroxy* pathways at the interface of phase  $\delta$  ( $\delta = g$  for gas or  $l$  for liquid) and transition-metal interfaces, as illustrated in Scheme 2a,b, respectively, by using Ru surfaces as an example.

During carbonyl hydrogenation in the  $\delta$  phase on transition-metal surfaces (Scheme 2), the carbonyl compound adsorbs as  $R_1C(O)R_2^*(\delta)$  and  $H_2(g)$  adsorbs dissociatively as H-adatoms ( $H^*(\delta)$ ), both in quasi-equilibrated steps (steps 2,i( $\delta$ ) and 2,ii( $\delta$ ), respectively). For the *Alkoxy* pathway (Scheme 2a),  $R_1C(O)R_2^*(\delta)$  may react with two H-adatoms consecutively via an initial, rapid C–H bond formation (step 2a,iii( $\delta$ ); barrier of 53–65 kJ mol<sup>−1</sup> on Ru(0001) under high vacuum for C<sub>1</sub>–C<sub>3</sub> aldehydes and C<sub>3</sub>–C<sub>4</sub> ketones<sup>1a</sup>), followed by a kinetically relevant homolytic O–H bond formation (step 2a,iv( $\delta$ ), barrier of 124–128 kJ mol<sup>−1</sup> on Ru(0001)<sup>1a</sup> under high vacuum),<sup>1a,17b</sup> forming  $R_1CH(OH)R_2^*(\delta)$ .

For the *Hydroxy* pathway (Scheme 2b),  $R_1C(O)R_2^*(\delta)$  may react with two H-adatoms via a homolytic O–H bond formation (step 2b,iii( $\delta$ ), barrier of 64–127 kJ mol<sup>−1</sup> on Ru(0001) under high vacuum<sup>1a</sup>) followed by a C–H bond formation (step 2b,iv( $\delta$ ), barrier of 70–90 kJ mol<sup>−1</sup> on Ru(0001) under high vacuum<sup>1a</sup>). DFT calculations have shown that the secondary C–H bond formation (i.e., step 2b,iv( $\delta$ )) is kinetically relevant for C<sub>1</sub>–C<sub>3</sub> aldehydes and C<sub>3</sub>–C<sub>4</sub> ketones on Ru(0001) under high vacuum for the *Hydroxy* pathway.<sup>1a</sup> Subsequently,  $R_1CH(OH)R_2(\delta)$  desorbs from the Ru surface in step 2,v( $\delta$ ). Equations 5a and 5b are the generalized equations that describe the enthalpy changes between the transition state of the kinetically relevant step and the reactant state ( $R_1C(O)R_2(\delta)$  and  $H_2(\delta)$ ) of the *Alkoxy* and *Hydroxy* pathways, i.e.,  $E_{Alkoxy,R_1C(O)R_2(\delta)}$  and  $E_{Hydroxy,R_1C(O)R_2(\delta)}$ , respectively, during carbonyl compound hydrogenation on uncovered Ru(0001) surfaces in the  $\delta$  phase:

**Scheme 2. Elementary Steps of Literature Proposed (a) Alkoxy Pathway<sup>1a,12a,17</sup> and (b) Hydroxy Pathway<sup>1a,12a,17</sup> during  $R_1C(O)R_2$  on Transition-Metal Surfaces in the  $\delta$  Phases ( $\delta = g, l$ ) and (c) Illustration of  $R_aC(O)H-L_2$  Reaction via the Alkoxy Pathway at  $L_2O$  and Transition Metal Interfaces<sup>a</sup>**



<sup>a</sup>Rate and equilibrium constants are directly labeled underneath/next to the step names.

$$E_{Alkoxy,R_1C(O)R_2(\delta)} = E\{[R_1CH(O\cdots H)R_2^*]^\ddagger(\delta)\} - E[H_2(g)] - E[R_1C(O)R_2(\delta)] \quad (5a)$$

$$E_{Hydroxy,R_1C(O)R_2(\delta)} = E\{[R_1C\cdots H(OH)R_2^*]^\ddagger(\delta)\} - E[H_2(g)] - E[R_1C(O)R_2(\delta)] \quad (5b)$$

where  $E_{i,R_1C(O)R_2(\delta)}$  denotes the activation enthalpy via pathway  $i$  ( $i = Alkoxy, Hydroxy$ ) and  $E[u(\delta)]$  ( $u = [R_1CH(O\cdots H)R_2^*]^\ddagger, [R_1C\cdots H(OH)R_2^*]^\ddagger, H_2, R_1C(O)R_2$ ) denotes the enthalpy of  $u$  in phase  $\delta$ .

For the Alkoxy pathway, the  $E_{Alkoxy,R_1C(O)R_2(\delta)}$  difference between the liquid phase and gas phase, by substituting  $\delta$  as  $l$  or  $g$  into eq 5a and taking the difference between  $E_{Alkoxy,R_1C(O)R_2(l)}$  and  $E_{Alkoxy,R_1C(O)R_2(g)}$  is

$$E_{Alkoxy,R_1C(O)R_2(l)} - E_{Alkoxy,R_1C(O)R_2(g)} = \Delta H_{sol,[R_1CH(O\cdots H)R_2^*]^\ddagger(g)} - \Delta H_{sol,R_1C(O)R_2(g)} \quad (6a)$$

where

$$\Delta H_{sol,u(g)} = E[u(l)] - E[u(g)] \quad (6b)$$

where  $\Delta H_{sol,u(g)}$  denotes the solvation enthalpy of gas-phase species  $u$  in the liquid phase. Similarly for the Hydroxy pathway, the  $E_{Hydroxy,R_1C(O)R_2(\delta)}$  difference between the liquid phase and gas phase, by substituting  $\delta$  as  $l$  or  $g$  into eq 5b and taking the difference between  $E_{Hydroxy,R_1C(O)R_2(l)}$  and  $E_{Hydroxy,R_1C(O)R_2(g)}$  is

$$E_{Hydroxy,R_1C(O)R_2(l)} - E_{Hydroxy,R_1C(O)R_2(g)} = \Delta H_{sol,[R_1C\cdots H(OH)R_2^*]^\ddagger(g)} - \Delta H_{sol,R_1C(O)R_2(g)} \quad (6c)$$

The solvation enthalpies of  $[R_1CH(O\cdots H)R_2^*]^\ddagger(g)$  and  $[R_1C\cdots H(OH)R_2^*]^\ddagger(g)$  must be similar due to their structural similarities. By taking the differences between eqs 6a and 6c, it leads to a constant difference in barrier for these pathways, irrespective of the solvation conditions:

$$E_{Alkoxy,R_1C(O)R_2(l)} - E_{Hydroxy,R_1C(O)R_2(l)} = E_{Alkoxy,R_1C(O)R_2(g)} - E_{Hydroxy,R_1C(O)R_2(g)} \quad (7)$$

At the interface between vapor and uncovered Ru(0001) surfaces, DFT calculations have shown that the Alkoxy pathway is a kinetically favorable pathway.<sup>1a</sup> We conclude, based on these theoretical calculations<sup>1a</sup> and eq 7, that the Alkoxy is the kinetically significant route, if  $H^*$  is the sole reactive hydrogen species, irrespective of the solvation conditions.

Contradictory to the finding above, we show that in  $H_2O$ , a protic solvent, Alkoxy pathway remains kinetically insignificant by carrying out  $R_aC(O)H-L_2-L_2O$  ( $R_a = n-C_3H_7$ ,  $L = H, D$ ) reactions on Ru surfaces at 323 K and probing their kinetic and isotopic implications. These isotopic studies, described next, confirm the dominance of an alternative pathway (i.e., the PET pathway in section 3.3) other than the Alkoxy and Hydroxy pathways described above. Reactions of  $R_aC(O)H$  ( $R_a = n-C_3H_7$ , denoted as I) and  $H_2$  in  $H_2O$  solvent on 1 wt % Ru/SiO<sub>2</sub> (1.8 nm average Ru cluster diameter) only leads to  $R_aCH_2OH$ , the hydrogenation product, whereas reactions of I and  $D_2$  in deuterium oxide ( $D_2O$ ) solvent form the exchange product,  $R_aC(O)D$  (II), in addition to the hydrogenation product,  $R_aCHDOD$  (III), at 323 K. Figure 5 shows the concentration of II versus III during I-D<sub>2</sub>-D<sub>2</sub>O reactions (0.04 M I, 1.3 bar of D<sub>2</sub>, 100 g of D<sub>2</sub>O, 50 mg of 1 wt % Ru/SiO<sub>2</sub>). The concentrations of II and III are linearly proportional to each other over a wide conversion range (0–30%). The instantaneous rate ratio of II to III,  $(r_{II}/r_{III})_{measured}$ , derived from the slope of Figure 5, is 0.75, a value that is smaller than unity.

Figure 6 shows the instantaneous concentrations of  $R_aCH_2OH$  versus that of  $R_aCHDOD$  (III) at identical reaction clock times, during two separate reaction experiments with either a  $R_aC(O)H$  (0.04 M)– $H_2$  (1.3 bar)– $H_2O$  or a  $R_aC(O)H$  (0.04 M)– $D_2$  (1.3 bar)– $D_2O$  mixture, respectively, in a gradientless batch-stirred tank reactor. The  $R_aCH_2OH$  and  $R_aCHDOD$  concentrations are linearly proportional to each other over a wide conversion range (0–30%). The slope of this plot reflects the rate ratio of  $R_aCH_2OH$  to  $R_aCHDOD$  (III) formation, i.e.,  $r_{R_aCH_2OH,Ru,H_2O} / (r_{R_aCHDOD,Ru,D_2O})^{-1}$ , and equals the observed, effective kinetic isotope effect ( $KIE_{obs}^{eff}$ ) of the  $R_aC(O)H$  hydrogenation reaction in the aqueous phase. Since this plot

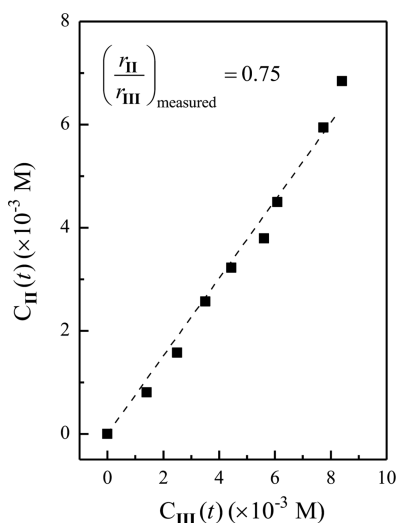


**Figure 5.** Linear relation between the instantaneous concentrations of  $n\text{-C}_3\text{H}_7\text{C}(\text{O})\text{D}$  (II),  $C_{\text{II}}(t)$ , and  $n\text{-C}_3\text{H}_7\text{CHDOD}$  (III),  $C_{\text{III}}(t)$ , during  $n\text{-C}_3\text{H}_7\text{C}(\text{O})\text{H}$  (I) reaction with  $\text{D}_2\text{-D}_2\text{O}$  (0.04 M  $n\text{-C}_3\text{H}_7\text{C}(\text{O})\text{H}$  and 1.3 bar  $\text{D}_2$ ) at 323 K on 50 mg of 1 wt % Ru/SiO<sub>2</sub> (1.8 nm average Ru cluster diameter). The dotted line is the best linear fit ( $R^2 = 0.998$ ).

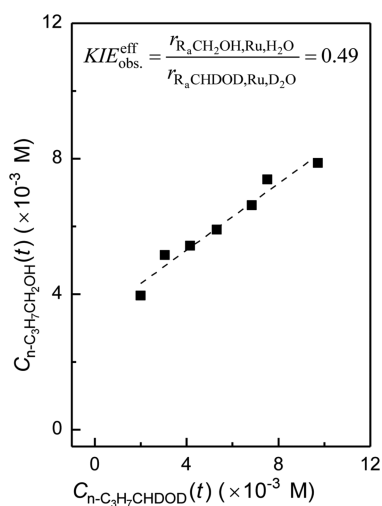


**Figure 6.** Linear relation between the instantaneous concentrations of  $n\text{-C}_3\text{H}_7\text{CH}_2\text{OH}$  ( $C_{n\text{-C}_3\text{H}_7\text{CH}_2\text{OH}}(t)$ ), measured during  $n\text{-C}_3\text{H}_7\text{C}(\text{O})\text{H-H}_2\text{-H}_2\text{O}$  reaction, and  $n\text{-C}_3\text{H}_7\text{CHDOD}$  ( $C_{n\text{-C}_3\text{H}_7\text{CHDOD}}(t)$ ), measured during  $n\text{-C}_3\text{H}_7\text{C}(\text{O})\text{H-D}_2\text{-D}_2\text{O}$  reaction, at the same reaction clock times on 1 wt % Ru/SiO<sub>2</sub> at 323 K (1.8 nm average Ru cluster diameter, 50 mg of catalyst, 0.04 M  $n\text{-C}_3\text{H}_7\text{C}(\text{O})\text{H}$ , 1.3 bar of  $\text{H}_2$  in  $\text{H}_2\text{O}$  or 1.3 bar  $\text{D}_2$  in  $\text{D}_2\text{O}$ ). The dotted line is the best linear fit ( $R^2 = 0.980$ ).

remains linear, the effective kinetic isotope effect remains constant with its value below unity at 0.49 ( $KIE_{\text{obs}}^{\text{eff}} = 0.49$ ) over the entire conversion range.

We first consider the *Alkoxy* pathway, interpreting the H–D isotopic exchange results and kinetic isotope effects within the framework of this pathway and then showing that these experimental results are inconsistent with the *Alkoxy* pathway. Scheme 2c is an extension of Scheme 2a, except that it also captures the individual steps during the H–D isotopic exchange reactions. It shows the sequence of  $\text{R}_a\text{C}(\text{O})\text{H}$  and  $L_2$  reactions in  $L_2\text{O}$  on Ru surfaces via the *Alkoxy* pathway; hereafter,  $L$  is either H or D. Steps  $L1$  and  $L2$  are counterparts of steps  $2_{\text{i}}(\delta)$  and  $2_{\text{ii}}(\delta)$  in  $L_2\text{-}L_2\text{O}$ , leading to the formation of  $\text{R}_a\text{C}(\text{O})\text{H}^*$  and

$L^*$ , respectively. Subsequently,  $L^*$  adds onto the carbonyl carbon of  $\text{R}_a\text{C}(\text{O})\text{H}^*$  (step  $L3$ ), forming  $\text{R}_a\text{CHLO}^*$  intermediates, followed by a second  $L^*$  addition onto the carbonyl oxygen to form  $\text{R}_a\text{CHLOL}^*$  (step  $L4$ ) that finally desorbs as the alcohol products (step  $L5$ ). The first H-addition step is quasi-equilibrated, and the second H-addition is kinetically relevant, irrespective of the identity of the reactive hydrogen species, as established previously via rate measurements<sup>17a</sup> and also consistent with results from first-principles calculations.<sup>12a</sup> If hydrogenation proceeds via the *Alkoxy* pathway (Scheme 2a,c), step  $L1$  must be reversible and lead the intermediates  $\text{R}_a\text{CHLO}^*$  to undergo (i) C–L bond cleavage (step C–L) that desorbs to recover  $\text{R}_a\text{C}(\text{O})\text{H}$  or (ii) C–H bond cleavage (step C–H) that desorbs to form H–L exchanged  $\text{R}_a\text{C}(\text{O})\text{L}$ . Steps C–L and C–H must both occur much more quickly than the kinetically relevant step, step  $L4$ .

In  $\text{H}_2\text{-H}_2\text{O}$ , step C–H is indistinguishable from step C–L; step  $L3$  and step C–L (or step C–H) are the forward and reverse reactions of  $\text{H}^*$  addition onto carbonyl carbon atom, respectively, and are quasi-equilibrated. In  $\text{D}_2\text{-D}_2\text{O}$ , however, step C–H, which proceeds much more quickly than step C–L due to the primary kinetic isotope effect, is irreversible, simply because the surfaces contain only  $\text{D}^*$  without any  $\text{H}^*$  in this case. Within this pathway, the formation of exchange product (II) must be much faster than that of hydrogenation product (III, step  $L4$ , Scheme 2c). Thus, when the *Alkoxy* pathway prevails, the exchange to hydrogenation rate ratio, i.e.,  $(r_{\text{II}}/r_{\text{III}})_{\text{Alkoxy}}$  must be much larger than unity. However, the measured  $(r_{\text{II}}/r_{\text{III}})_{\text{measured}}$  ratio is 0.75. Although the initial  $\text{H}^*$  addition onto carbonyl carbon does occur and forms  $\text{R}_a\text{CHLO}^*$  intermediates (Figure 5), they remain as the spectator species. On the basis of these results, we conclude that the *Alkoxy* pathway is not the dominant hydrogenation pathway.

Assuming that the coverages on Ru surfaces remain identical in  $\text{H}_2\text{-H}_2\text{O}$  and  $\text{D}_2\text{-D}_2\text{O}$  mixtures, the effective kinetic isotope effect of  $\text{R}_a\text{C}(\text{O})\text{H}$  and  $\text{H}_2$  reactions via the *Alkoxy* pathway ( $KIE_{\text{Alkoxy}}^{\text{eff}}$ ) depends on the equilibrium isotope effect of step  $Lx$  ( $EIE_{Lx}$ ,  $x = 2, 3$ ) and kinetic isotope effects of  $\text{H}^*$  addition onto carbonyl oxygen ( $KIE_{L4}$ , step  $L4$ ) and of C–L bond cleavage ( $KIE_{C-L}$ , step C–L) (derivation in Section S2 of the Supporting Information):

$$KIE_{\text{Alkoxy}}^{\text{eff}} = EIE_{L2}EIE_{L3}KIE_{L4}(1 + KIE_{C-L}) \quad (8a)$$

where

$$EIE_{Lx} = \frac{K_{\text{H}x}}{K_{\text{D}x}} \quad (8b)$$

$$KIE_{L4} = \frac{k_{\text{H}4}}{k_{\text{D}4}} \quad (8c)$$

$$KIE_{C-L} = \frac{k_{C-H}}{k_{C-D}} \quad (8d)$$

where  $k_y$  and  $K_y$  denote the rate and equilibrium constants of step  $y$  ( $y = Lx, C-L, x = 2-4$ , Scheme 2c). These equilibrium and kinetic isotope effects of elementary steps in the aqueous phase (Scheme 2c) must be comparable with those of their gas-phase counterparts, as  $\text{H}_2\text{O}$  and  $\text{D}_2\text{O}$  do not participate in the *Alkoxy* pathway (Scheme 2a,c) and the solvation of enthalpy and entropy of  $[\text{R}_1\text{CH}(\text{O}\cdots\text{H})\text{R}_2^*]^\ddagger$ ,  $[\text{R}_1\text{C}\cdots\text{H}(\text{OH})\text{R}_2^*]^\ddagger$ , or  $\text{R}_1\text{C}(\text{O})\text{R}_2$  must remain similar in either  $\text{H}_2\text{O}$  or  $\text{D}_2\text{O}$ . Table 2 summarizes the individual equilibrium isotope or kinetic

isotope effects and the overall, effective kinetic isotope effect for *Alkoxy* pathway.

**Table 2. Summary of the Equilibrium Isotope Effects and Kinetic Isotope Effects of the Elementary Steps for *Alkoxy* (Scheme 2c) and PET (Scheme 3) Pathways and the Expected Effective Kinetic Isotope Effects for *Alkoxy* (Calculated on the Basis of Eq 8a) and PET (Calculated on the Basis of Eq 15) Pathways during Hydrogenation of Carbonyls on Ru Clusters at 323 K**

pathway	elementary step	equilibrium isotope effect (EIE)	kinetic isotope effect (KIE)	expected effective KIE
<i>Alkoxy</i> <sup>a</sup>	L2	0.7 <sup>c</sup>		
	L3	~2.4 <sup>e</sup>		3.4–114
	L4		1.0–11.7 <sup>d</sup>	
	C–L		1.0–4.8 <sup>e</sup>	
PET <sup>b</sup>	2	0.7 <sup>c</sup>		
	3 and 4	~0.5 <sup>f</sup>		0.35–4.10
	5a		1.0–11.7 <sup>g</sup>	

<sup>a</sup>Elementary steps of *Alkoxy* pathway in Scheme 2c. <sup>b</sup>Elementary steps of PET pathway in Scheme 3. <sup>c</sup>Calculated on the basis of eq 9. <sup>d</sup>Calculated on the basis of eq 12a. <sup>e</sup>Calculated on the basis of eq 12b. <sup>f</sup>Estimated on the basis of the enthalpy contribution in the equilibrium isotope effect of ionic O–H<sup>+</sup> bond formation. <sup>g</sup>Estimated on the basis of the activation enthalpy contribution in the kinetic isotope effect of H to Ru(surface) bond rupture (appears comparable with step L4 of Scheme 2c, Section 3.2).

When  $K_{Lx}$  is expressed as free energy changes ( $\Delta G_{Lx}$ ) and then as enthalpic ( $\Delta H_{Lx}$ ) and entropic ( $\Delta S_{Lx}$ ) changes, eq 8b becomes

$$\begin{aligned} EIE_{Lx} &= \frac{K_{Hx}}{K_{Dx}} = \frac{\exp\{-\Delta G_{Hx}/RT\}}{\exp\{-\Delta G_{Dx}/RT\}} \\ &= \exp\left\{-\frac{(\Delta H_{Hx} - \Delta H_{Dx})}{RT}\right\} \exp\left\{\frac{(\Delta S_{Hx} - \Delta S_{Dx})}{R}\right\} \end{aligned} \quad (9)$$

At gas and Ru interfaces, a literature report has stated that the enthalpy and entropy for dissociative H<sub>2</sub> adsorption are 5.6 kJ mol<sub>H<sub>2</sub></sub><sup>-1</sup> and 14.4 J mol<sub>H<sub>2</sub></sub><sup>-1</sup> K<sup>-1</sup> more positive than those of D<sub>2</sub>, respectively.<sup>18</sup> Substituting these values into eq 9 leads the estimated  $EIE_{L2}$  to be 0.7 at 323 K (Table 2). In fact, the reaction enthalpy difference between steps H<sub>2</sub> and D<sub>2</sub> (5.6 kJ mol<sup>-1</sup>)<sup>18</sup> and the heat of formation of H atom (218 kJ mol<sup>-1</sup>)<sup>19</sup> and D atom (221.72 kJ mol<sup>-1</sup>)<sup>19</sup> provide an evaluation of the zero-point energy difference between Ru–H ( $ZPE_{Ru-H}$ ) and Ru–D bonds ( $ZPE_{Ru-D}$ ), i.e.,  $ZPE_{Ru-H} - ZPE_{Ru-D}$ , values of 6.6 kJ mol<sup>-1</sup> (see derivation in Section S2 of Supporting Information).

For the equilibrium isotope effect of step L3, which involves C–L bond formation, the enthalpic difference between steps H3 and D3,  $\Delta H_{H3} - \Delta H_{D3}$ , is

$$\begin{aligned} \Delta H_{H3} - \Delta H_{D3} &= (ZPE_{C-H} - ZPE_{Ru-H}) - (ZPE_{C-D} - ZPE_{Ru-D}) \\ &= (ZPE_{C-H} - ZPE_{C-D}) - (ZPE_{Ru-H} - ZPE_{Ru-D}) \end{aligned} \quad (10)$$

Substituting the zero-point energy difference between C–H ( $ZPE_{C-H}$ ) and C–D ( $ZPE_{C-D}$ ) bonds (~4.2 kJ mol<sup>-1</sup>, calculated

on the basis of the bond dissociation energy difference between H<sub>3</sub>C–H and H<sub>3</sub>C–D bonds)<sup>20</sup> and the zero-point energy difference between Ru–H and Ru–D bond (6.6 kJ mol<sup>-1</sup>) into eq 10 leads to the enthalpic difference between steps H3 and D3, i.e.,  $\Delta H_{H3} - \Delta H_{D3}$ , of –2.4 kJ mol<sup>-1</sup>. We neglect the entropic contribution (i.e., the term  $\exp\{(\Delta S_{H3} - \Delta S_{D3})/R\}$ ) from eq 9, as the entropic contribution of similar H\* addition onto the carbon atom of CO on Co(0001) and Fe(110) remains insignificant and close to unity (entropic contributions of 1.06 and 1.08, respectively).<sup>21</sup> Therefore, the  $\Delta H_{H3} - \Delta H_{D3}$  value of –1.8 kJ mol<sup>-1</sup> and eq 9 leads to the estimated equilibrium isotope effect of step L3–2.4 at 323 K (Table 2).

On expansion of the rate constants according to the Eyring equation, eqs 8c and 8d become

$$\begin{aligned} KIE_{L4} &= \frac{k_{H4}}{k_{D4}} = \frac{\exp\{-\Delta G_{H4}^\ddagger/RT\}}{\exp\{-\Delta G_{D4}^\ddagger/RT\}} \\ &= \exp\left\{-\frac{(\Delta H_{H4}^\ddagger - \Delta H_{D4}^\ddagger)}{RT}\right\} \exp\left\{\frac{(\Delta S_{H4}^\ddagger - \Delta S_{D4}^\ddagger)}{R}\right\} \end{aligned} \quad (11a)$$

$$\begin{aligned} KIE_{C-L} &= \frac{k_{C-H}}{k_{C-D}} = \frac{\exp\{-\Delta G_{C-H}^\ddagger/RT\}}{\exp\{-\Delta G_{C-D}^\ddagger/RT\}} \\ &= \exp\left\{-\frac{(\Delta H_{C-H}^\ddagger - \Delta H_{C-D}^\ddagger)}{RT}\right\} \\ &\quad \exp\left\{\frac{(\Delta S_{C-H}^\ddagger - \Delta S_{C-D}^\ddagger)}{R}\right\} \end{aligned} \quad (11b)$$

where  $\Delta G_y^\ddagger$ ,  $\Delta H_y^\ddagger$ , and  $\Delta S_y^\ddagger$  denote the free energy, enthalpy, and entropy of activation for step  $y$  ( $y = L4, C-L$ , Scheme 2c), respectively. On Co(0001) and Fe(110) surfaces, a literature report has stated that the differences in activation entropy between H\* addition and D\* addition onto the oxygen atom of surface HCO\* species are negligible (<1 J mol<sup>-1</sup> K<sup>-1</sup>).<sup>21</sup> These H\* addition and D\* addition steps on oxygen atoms<sup>21</sup> are comparable with steps H4 and D4, respectively. Thus, we expect that the activation entropy changes for steps L4 and C–L, when protium is replaced with deuterium, remain insignificant (i.e.,  $\Delta S_{H4}^\ddagger - \Delta S_{D4}^\ddagger \approx 0$ ;  $\Delta S_{C-H}^\ddagger - \Delta S_{C-D}^\ddagger \approx 0$ ). Neglecting this entropic variation, eqs 11a and 11b become

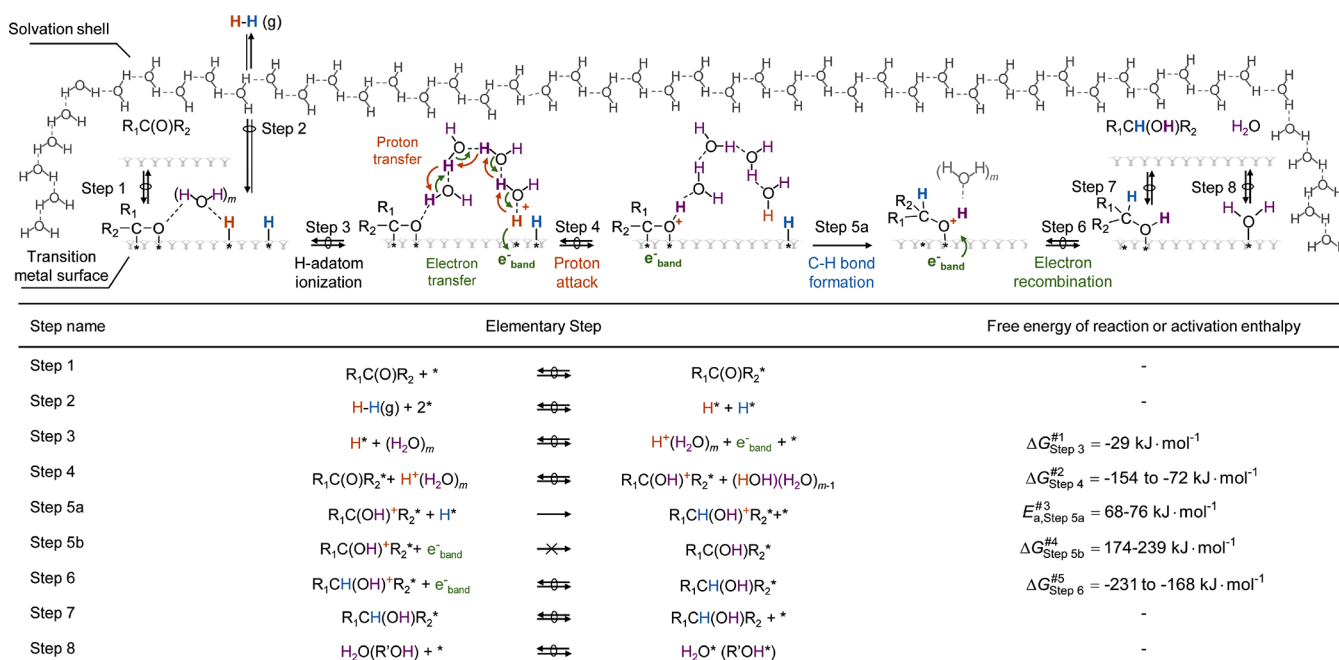
$$KIE_{L4} = \frac{k_{H4}}{k_{D4}} \approx \exp\left\{-\frac{(\Delta H_{H4}^\ddagger - \Delta H_{D4}^\ddagger)}{RT}\right\} \quad (12a)$$

$$KIE_{C-L} = \frac{k_{C-H}}{k_{C-D}} \approx \exp\left\{-\frac{(\Delta H_{C-H}^\ddagger - \Delta H_{C-D}^\ddagger)}{RT}\right\} \quad (12b)$$

where

$$\begin{aligned} \Delta H_{H4}^\ddagger - \Delta H_{D4}^\ddagger &= (ZPE_{Ru\cdots H\cdots O}^\ddagger - ZPE_{Ru-H}^\ddagger) - (ZPE_{Ru\cdots D\cdots O}^\ddagger \\ &\quad - ZPE_{Ru-D}^\ddagger) \\ &= (ZPE_{Ru\cdots H\cdots O}^\ddagger - ZPE_{Ru\cdots D\cdots O}^\ddagger) \\ &\quad - (ZPE_{Ru-H}^\ddagger - ZPE_{Ru-D}^\ddagger) \end{aligned} \quad (12c)$$

and

**Scheme 3. Proposed Sequence of Elementary Steps during  $R_1C(O)R_2$  Hydrogenation at Protic Solvent and Transition Metal Interfaces via Proton–Electron Transfer (PET), Illustrated Using the  $H_2O$ –Ru Interface as an Example**


#1: Free energy derivation in Section S7 of Supporting Information.

#2: Free energy derivation in Section S4 of Supporting Information.

#3: Density functional theory calculations on Ru(0001) from literature.<sup>1a,12a</sup>

#4: Free energy derivation in Section S5 of Supporting Information.

#5: Free energy derivation in Section S6 of Supporting Information.

(\* refers to metal site,  $\rightleftharpoons$ ,  $\rightarrow$ ,  $\nrightarrow$ , and  $\cdots$  denote a quasi-equilibrated step, an irreversible step, a kinetically unfeasible step, and an intermolecular hydrogen bond, respectively.)

$$\begin{aligned} \Delta H_{C-H}^{\ddagger} - \Delta H_{C-D}^{\ddagger} &= (ZPE_{C-H \cdots Ru}^{\ddagger} - ZPE_{C-H}) - (ZPE_{C-D \cdots Ru}^{\ddagger} - ZPE_{C-D}) \\ &= (ZPE_{C-H \cdots Ru}^{\ddagger} - ZPE_{C-D \cdots Ru}^{\ddagger}) - (ZPE_{C-H} - ZPE_{C-D}) \end{aligned} \quad (12d)$$

where  $ZPE_{Ru \cdots L \cdots O}^{\ddagger}$  and  $ZPE_{C \cdots L \cdots Ru}^{\ddagger}$  denote the zero-point energies of transition states of step  $L4$  and step  $C-L$ , respectively. Due to the antisymmetrical vibration in the transition state (i.e., the force constants of  $C-H$  or  $O-H$  bonds differ from that of the  $Ru-H$  bond),<sup>22</sup> the magnitude of the primary kinetic isotope effect depends on the lateness of the transition state,<sup>22</sup> which ranges from a minimum value of unity for an early transition state to a maximum, occurring when the zero-point energy difference between H atom and D atom transfer vanishes at the transition state for  $Ru \cdots L \cdots O$  or  $C \cdots L \cdots Ru$ . From the zero-point energy difference between  $Ru-H$  and  $Ru-D$  bonds ( $ZPE_{Ru-H} - ZPE_{Ru-D}$ ) of  $6.6 \text{ kJ mol}^{-1}$  and that between  $C-H$  and  $C-D$  bonds ( $ZPE_{C-H} - ZPE_{C-D}$ ) of  $\sim 4.2 \text{ kJ mol}^{-1}$ ,<sup>20</sup> we estimate that the primary kinetic isotope effects of step  $L4$  range from 1.0 to 11.7 (Table 2) and those of step  $C-L$  range from 1.0 to 4.8 (Table 2) at 323 K. Substituting the equilibrium isotope effects of steps  $L2$  (0.7) and  $L3$  ( $\sim 2.4$ ) and the kinetic isotope effects of steps  $L4$  (1.0–11.7) and  $C-L$  (1.0–4.8) into eq 8a leads to the expected range of effective kinetic isotope effect for the *Alkoxy* pathway ( $KIE_{Alkoxy}^{eff}$ ) from 3.4 to 114 at 323 K, as summarized in Table 2; these expected values are larger than unity and are much larger than the observed values ( $KIE_{obs}^{eff} = 0.49$ , Figure 6). Since both the effective kinetic isotope effects and the measured exchange to hydrogenation rate ratio for carbonyl hydrogenation in protic solvents are inconsistent with those of the *Alkoxy* pathway, this pathway cannot be the prevalent mechanism.

**3.3. Elementary Steps and Rate Expressions for Carbonyl Hydrogenation Reactions at the Interface of Protic Solvent and Transition Metal.** Here, we propose a proton–electron transfer pathway (PET pathway) and its associated sequence of elementary steps that capture the reactivity trends among the carbonyls (Figures 1a and 4) and with changing solvent identities (Figure 1b), consistent with the measured exchange to hydrogenation rate ratio ( $(r_{II}/r_{III})_{measured}$ , Figure 5), effective kinetic isotope effects of the hydrogenation reaction with  $n-C_3H_7C(O)H-H_2-H_2O$  and  $n-C_3H_7C(O)H-D_2-D_2O$  mixtures (Figure 6), and energetics derived from first-principles calculations<sup>12a</sup> during  $C_2H_5C(O)CH_3$  hydrogenation on Ru(0001) surfaces, when such surfaces are in contact with protic solvent.

Scheme 3 shows the proposed sequence of elementary steps that depicts the  $C=O$  bond hydrogenation at such interfaces, illustrated with an  $H_2O$ –Ru interface as an example. Hereafter, we abbreviate all species, which include nonadsorbed molecules and adsorbed surface species, as “z” in the condensed phase and “z(g)” in the gas phase. On transition-metal surfaces, water molecules form a bilayer structure,<sup>9,23</sup> carbonyl compounds adsorb as  $R_1C(O)R_2^*$ , and  $H_2(g)$  molecules dissociate as  $H^*$  adatoms in quasi-equilibrated steps (steps 1 and 2).<sup>1a,12a,b</sup> The  $H^*$  becomes ionized by transferring its electron into the metal’s d band, forming a solvated proton ( $H^+(H_2O)_m$ ,  $m \geq 1$ , step 3). This ionization step is mechanistically analogous to the Volmer step during the electrochemical oxidation of an H-adatom (forward direction) under “open-circuit” conditions:



The intrinsic forward rates for the Volmer step (eq 13), extrapolated from the exchange current densities ( $i_0$ ) at zero overpotential on Ru, Pt, and Pd polycrystalline surfaces, are at

least 1 order of magnitude larger than the highest hydrogenation turnover rate measured in this study (e.g., rates of Volmer step vs hydrogenation reaction are 5.0 vs 0.1 mol<sub>H</sub> g atom<sub>surf,Pt</sub><sup>-1</sup> s<sup>-1</sup> on Pt, Section S3 in the Supporting Information).<sup>4</sup> Thus, the formation of a proton and an electron pair is fast and quasi-equilibrated (step 3).

The resulting proton in H<sup>+</sup>(H<sub>2</sub>O)<sub>m</sub> (*m* ≥ 1) attacks the carbonyl oxygen of R<sub>1</sub>C(O)R<sub>2</sub><sup>\*</sup>, forming R<sub>1</sub>C(OH)<sup>+</sup>R<sub>2</sub><sup>\*</sup> in step 4. The proton transfer from H<sup>+</sup>(H<sub>2</sub>O)<sub>m</sub> to R<sub>1</sub>C(O)R<sub>2</sub><sup>\*</sup> resembles the proton exchange among oxoacids, the rate of which reaches the diffusion limit of H<sup>+</sup> in the aqueous phase (~10<sup>10</sup> M<sup>-1</sup> s<sup>-1</sup> at 298 K).<sup>24</sup> The free energy of the proton transfer from H<sup>+</sup>(H<sub>2</sub>O)<sub>m</sub> to R<sub>1</sub>C(O)R<sub>2</sub><sup>\*</sup> is negative (from -154 to -72 kJ mol<sup>-1</sup>, Section S4 in the Supporting Information). Thus, this step occurs rapidly and reaches chemical equilibrium. The net consequence is the formation of an ionic O-H<sup>+</sup> bond, mechanistically different from the formation of a covalent O-H or C-H bond via the direct addition of an H-atom to R<sub>1</sub>C(O)R<sub>2</sub><sup>\*</sup>(g) prevalent at the gas-Ru(0001) interface (Scheme 2a,b).<sup>1a</sup> A sequential H<sup>\*</sup> addition to R<sub>1</sub>C(OH)<sup>+</sup>R<sub>2</sub><sup>\*</sup> forms a C-H bond and leads to a charged alcohol (R<sub>1</sub>CH(OH)<sup>+</sup>R<sub>2</sub><sup>\*</sup>) intermediate in step 5a. We neglect the possibility of proton addition during this C-H bond formation, as the positively charged R<sub>1</sub>C(OH)<sup>+</sup>R<sub>2</sub><sup>\*</sup> intermediates repel the positively charged proton species. First-principles calculations have shown that the direct H<sup>\*</sup> addition to the C<sup>1</sup> atom of the charged C<sub>2</sub>H<sub>5</sub>C<sup>1</sup>(OH)<sup>δ+</sup>CH<sub>3</sub><sup>\*</sup> species has a barrier of 68–70 kJ mol<sup>-1</sup> in H<sub>2</sub>O or isopropyl alcohol solvent.<sup>12a</sup> This barrier is similar to the homolytic C-H bond formation between H<sup>\*</sup>(g) and noncharged C<sub>2</sub>H<sub>5</sub>C(OH)CH<sub>3</sub><sup>\*</sup>(g) species in the gas phase (72 kJ mol<sup>-1</sup>).<sup>1a,12a</sup> The barriers remaining largely constant, irrespective of the reaction media (both gas-metal and liquid-metal interfaces) further confirms that step 5a involves a homolytic C-H bond formation, during which the H-atom directly reacts with the C<sup>1</sup> atom of R<sub>1</sub>C<sup>1</sup>(OH)<sup>+</sup>R<sub>2</sub><sup>\*</sup> and forms a covalent C-H bond. This barrier also remains largely independent of the carbon number of R<sub>1</sub>C(OH)R<sub>2</sub><sup>\*</sup>(g) (R<sub>1</sub> = C<sub>n</sub>H<sub>2n+1</sub> (*n* = 2–4) and R<sub>2</sub> = H; alternatively, R<sub>1</sub> = CH<sub>3</sub>, C<sub>2</sub>H<sub>5</sub> and R<sub>2</sub> = CH<sub>3</sub>) at 70–76 kJ mol<sup>-1</sup>.<sup>1a,12a</sup> We exclude the alternate route (step 5b), through which R<sub>1</sub>C(OH)<sup>+</sup>R<sub>2</sub><sup>\*</sup> may recombine with an electron in the metal band (e<sup>-</sup><sub>band</sub>) to form a noncharged R<sub>1</sub>C(OH)R<sub>2</sub><sup>\*</sup> species, because this step has an exceptionally high positive free energy change (>174 kJ mol<sup>-1</sup>, derived in Section S5 in the Supporting Information) and would lead to rates largely independent of P<sub>R<sub>1</sub>C(O)R<sub>2</sub>(g)</sub>.

After the kinetically relevant formation of R<sub>1</sub>CH(OH)<sup>+</sup>R<sub>2</sub><sup>\*</sup>, it recombines with an electron from the metal's d band (e<sup>-</sup><sub>band</sub>) in a thermodynamically preferable step with free energy changes ranging from -231 to -168 kJ mol<sup>-1</sup> (step 6, Section S6 in the Supporting Information) for the various R<sub>1</sub>CH(OH)<sup>+</sup>R<sub>2</sub><sup>\*</sup> species. The resulting R<sub>1</sub>CH(OH)R<sub>2</sub><sup>\*</sup> binds weakly to the transition metals (e.g., -41 to -21 kJ mol<sup>-1</sup> for C<sub>1</sub>–C<sub>4</sub> alkanols on uncovered Ru(0001)<sup>1a</sup>) and desorbs to complete the catalytic cycle (step 7). During steady-state catalysis, solvent molecules R'OH (in this case H<sub>2</sub>O) competitively adsorb and titrate the vacant Ru sites in a quasi-equilibrated step (step 8).

In comparison with the *Alkoxy* pathway, the activation enthalpy between the transition state and the reactant state for the PET pathway is much lower,<sup>12a</sup> by 88–238 kJ mol<sup>-1</sup> (Scheme 2a, derived in Section S7 in the Supporting Information). In D<sub>2</sub>-D<sub>2</sub>O, hydrogenation of aldehydes (e.g., R<sub>a</sub>C(O)H) via the PET pathway does not form an H-D

exchange product (i.e., R<sub>a</sub>C(O)D), because the kinetically relevant C-H bond formation is irreversible (step 5a). The observed H-D exchange on a carbonyl carbon atom (Figure 5) occurs via the formation of the R<sub>a</sub>CHDO<sup>\*</sup> intermediate but mainly as a spectator species (Scheme 2c), because the hydrogenation rate arising from the *Alkoxy* pathway must be much smaller than 7%, computed on the basis of the exchange to hydrogenation rate ratio of the *Alkoxy* pathway of ~10 measured during gas-phase butanal hydrogenation on Ru/SiO<sub>2</sub> (1 wt %, ~2 nm Ru cluster) at 323 K (butanal and H<sub>2</sub> partial pressures of 0.2 and 40 kPa, respectively). As a result, the observed hydrogenation rate must predominantly come from the PET pathway, which exceeds the H-D exchange rate, leading the measured exchange to hydrogenation rate ratio to be smaller than unity ((*r*<sub>II</sub>/*r*<sub>III</sub>)<sub>measured</sub> = 0.75, Figure 5).

The sequence of elementary steps and pseudo-steady-state treatment of all surface intermediates *z*<sup>\*</sup> (*z* = H, R'OH, R<sub>1</sub>C(O)R<sub>2</sub>, R<sub>1</sub>C(OH)<sup>+</sup>R<sub>2</sub>, R<sub>1</sub>CH(OH)<sup>+</sup>R<sub>2</sub>, R<sub>1</sub>CH(OH)R<sub>2</sub>) in Scheme 3 lead to the turnover rate expression for condensed-phase hydrogenation:

$$-r_{R_1C(O)R_2,M,I} = (K_1K_2K_3K_4)k_{sa}\theta_s^2C_{R_1C(O)R_2}P_{H_2} \quad (14)$$

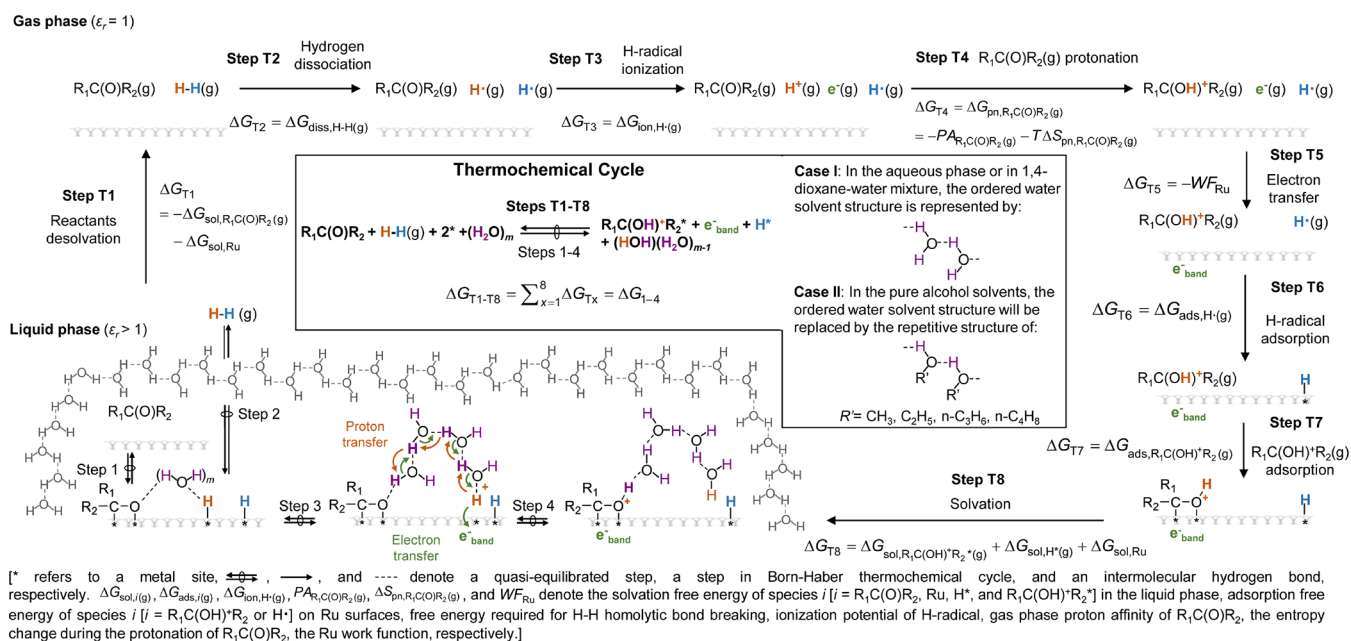
where *P*<sub>H<sub>2</sub></sub>, *k*<sub>sa</sub>, and *K*<sub>*x*</sub> (*x* = 1–4) denote the H<sub>2</sub> pressure (evaluated at 323 K), the elementary rate constant for C-H bond formation in step 5a, and the equilibrium constant of step *x* in Scheme 3, respectively.

Assuming that the coverages on Ru surfaces remain identical in H<sub>2</sub>-H<sub>2</sub>O and D<sub>2</sub>-D<sub>2</sub>O mixtures, the effective kinetic isotope effect of R<sub>a</sub>C(O)H-H<sub>2</sub> reactions via the PET pathway (*KIE*<sub>PET</sub><sup>eff</sup>) depends on the equilibrium isotope effect of steps 2–4 (*EIE*<sub>*x*</sub>, *x* = 2, 3) and kinetic isotope effect of H<sup>\*</sup> addition onto the carbonyl carbon (*KIE*<sub>sa</sub>, step 5a):

$$KIE_{PET}^{eff} = EIE_2EIE_3EIE_4KIE_{sa} \quad (15)$$

The equilibrium isotope effect of step 2 is equivalent to the equilibrium isotope effect of step L2 (Scheme 2c), which is 0.7 at 323 K on Ru (eq 9, Section 3.2), as summarized in Table 2. The equilibrium isotope effect of proton transfer reactions in the homogeneous phase is much smaller than unity (0.1–0.8, 288–373 K),<sup>25</sup> because charged intermediates formed via deuterium transfer in D<sub>2</sub>O are more stable than those via proton transfer in H<sub>2</sub>O. The zero-point energy difference between a single ionic O-H<sup>+</sup> bond of H<sub>3</sub>O<sup>+</sup> and O-D<sup>+</sup> bond of H<sub>2</sub>DO<sup>+</sup> (*ZPE*<sub>O-H<sup>+</sup></sub> - *ZPE*<sub>O-D<sup>+</sup></sub>) is ~8.45 kJ mol<sup>-1</sup> (excluding hydrogen-bond contributions).<sup>26</sup> From the zero-point energy difference between Ru-H and Ru-D bonds (*ZPE*<sub>Ru-H</sub> - *ZPE*<sub>Ru-D</sub>) of 6.6 kJ mol<sup>-1</sup> and the zero-point energy difference between O-H<sup>+</sup> and O-D<sup>+</sup> bonds (*ZPE*<sub>O-H<sup>+</sup></sub> - *ZPE*<sub>O-D<sup>+</sup></sub>) of 8.45 kJ mol<sup>-1</sup>, we estimate the product of equilibrium isotope effect of steps 3 and 4, i.e., *EIE*<sub>3</sub>*EIE*<sub>4</sub>, to be ~0.5 at 323 K by neglecting the entropic contribution (Table 2). These *EIE*<sub>*x*</sub> (*x* = 2–4) values and the estimated kinetic isotope effect of step 5a, ranging from 1.0 to 11.7 (Table 2), lead to the expected effective kinetic isotope effect value of 0.35–4.10 for the PET pathway (*KIE*<sub>PET</sub><sup>eff</sup> = 0.35–4.10, Table 2), consistent with the observed low kinetic isotope effect, which is much smaller than unity, of 0.49 measured with *n*-C<sub>3</sub>H<sub>7</sub>C(O)H-H<sub>2</sub>-H<sub>2</sub>O and *n*-C<sub>3</sub>H<sub>7</sub>C(O)H-D<sub>2</sub>-D<sub>2</sub>O mixtures at 323 K (Figure 6, Section 3.2). To summarize, the much lower apparent activation barrier and the measured exchange to hydrogenation rate ratio and effective H-D kinetic isotope effects both meeting those expected for PET pathway, taken together, confirm that the PET pathway must be the dominant

### Scheme 4. Born–Haber Thermochemical Construct as an Alternative Path for the Quasi-Equilibrated Steps 1–4 of Scheme 3 at the Interface of Protic Solvent and Ru Metal



hydrogenation route. The other two pathways (Section 3.2), which exhibit much higher apparent barriers, exchange to hydrogenation ratios, and effective kinetic isotope effects, are unlikely to be the prevalent paths.

After comparison of eq 14 with eqs 1b and 1c, the first-order rate coefficient,  $k_{R_1C(O)R_2,M,1}^{1st}$  is

$$k_{R_1C(O)R_2,M,1}^{1st} = (K_1K_2K_3K_4)k_{5a}\theta_*^2P_{H_2} \quad (16a)$$

and the lumped rate constant,  $k_{R_1C(O)R_2,M,1}^{lumped}$  and  $f_{R_1C(O)R_2,M,1}(\theta_*, P_{H_2})$  are

$$k_{R_1C(O)R_2,M,1}^{lumped} = (K_1K_2K_3K_4)k_{5a} \quad (16b)$$

$$f_{R_1C(O)R_2,M,1}(\theta_*, P_{H_2}) = \theta_*^2P_{H_2} \quad (16c)$$

Competitive hydrogenation of carbonyl pairs reflects the trends in lumped rate constant without its influence by  $\theta_*$  (eq 16b, Figure 4), which remain identical with those in first-order rate coefficient, which contains effects from  $\theta_*$  (eq 16a, Figure 1a). Therefore, the term  $\theta_*^2P_{H_2}$  (captured in  $f_{R_1C(O)R_2,M,1}(\theta_*, P_{H_2})$ , eq 16c) must remain largely constant across the carbonyl series and with different solvents, as protic solvent molecules adsorb weakly on metal surfaces (e.g., heats of R'OH adsorption are all around  $32 \pm 10$  kJ mol<sup>-1</sup> on Ru(0001),<sup>1a,23b</sup>). According to eqs 16a–16c, the variation in  $k_{R_1C(O)R_2,M,1}^{1st}$  reflects that in  $k_{R_1C(O)R_2,M,1}^{lumped}$ , i.e.,  $\Delta_y[k_{R_1C(O)R_2,M,1}^{1st}]$  relates to  $\Delta_y[k_{R_1C(O)R_2,M,1}^{lumped}]$  via:

$$\Delta_y[k_{R_1C(O)R_2,M,1}^{1st}] = \theta_*^2P_{H_2}\Delta_y[k_{R_1C(O)R_2,M,1}^{lumped}] = \theta_*^2P_{H_2}\Delta_y[(K_1K_2K_3K_4)k_{5a}] \quad (17)$$

Since the barrier and rate constant  $k_{5a}$  for C–H bond formation (step 5a) remain largely insensitive to the identity of aliphatic carbonyl and solvent (68–76 kJ mol<sup>-1</sup> on Ru(0001) under vacuum<sup>1a,12a</sup> or in H<sub>2</sub>O<sup>12a</sup> or isopropyl alcohol<sup>12a</sup>), the variation in  $k_{R_1C(O)R_2,M,1}^{1st}$  reflects predominantly the change in the

equilibrium constant term ( $K_1K_2K_3K_4$ ), which captures the free energy difference between steps 1 and 4 ( $\Delta G_{1-4}$ , Scheme 3) for aliphatic carbonyls:

$$\Delta_y[k_{R_1C(O)R_2,M,1}^{1st}] = k_{5a}\theta_*^2P_{H_2}\Delta_y[(K_1K_2K_3K_4)] = k_{5a}\theta_*^2P_{H_2}\Delta_y\left[\exp\left(-\frac{\Delta G_{1-4}}{RT}\right)\right] \quad (18)$$

Acetophenone, however, exhibits a higher first-order rate coefficient and lumped rate constant in comparison to the predicted values on the basis of the trend line generated from the aliphatic carbonyl series (Figure 2b); this higher rate coefficient is potentially caused by the presence of aromaticity that stabilizes the C–H bond formation transition state.

In what follows, we construct a Born–Haber thermochemical cycle to interpret the free energy changes for these quasi-equilibrated steps (steps 1–4 of Scheme 3),  $\Delta G_{1-4}$ , before the kinetically relevant C–H bond formation for aliphatic carbonyls.

**3.4. Born–Haber Thermochemical Construct Capturing the Reactant and Solvent Identity Effects on Hydrogenation Rate Constants.** The free energy change between steps 1 and 4 of Scheme 3,  $\Delta G_{1-4}$ , is a state function between the final state of  $R_1C(OH)^+R_2^*$ ,  $H^*$ , and Ru surface (with  $e^-_{band}$ ) and the initial state of  $R_1C(O)R_2$ ,  $H_2(g)$ , and Ru surface (without  $e^-_{band}$ ). For this reason, any hypothetical paths linking the two states can describe  $\Delta G_{1-4}$  entirely. Scheme 4 shows a Born–Haber thermochemical construct that captures this free energy change with a plausible set of hypothetical paths. These paths begin with the removal of  $R_1C(O)R_2$  and Ru surface from the condensed phase ( $\epsilon_r > 1$ ) into the gas phase ( $\epsilon_r = 1$ , step T1). Subsequently,  $H_2(g)$  undergoes homolytic dissociation, forming two H-radicals ( $H\cdot(g)$ , step T2). One of the H-radicals ionizes to form a proton and electron pair ( $H^+(g)$  and  $e^-(g)$ , step T3). The proton then attacks the C=O bond of  $R_1C(O)R_2(g)$ , forming  $R_1C(OH)^+R_2(g)$  (step T4). The electron transfers to Ru's d band (as in  $e^-_{band}$ , step T5). The other H-radical adsorbs on Ru surfaces and forms an H-atom

( $H^*(g)$ , step T6).  $R_1C(OH)^+R_2(g)$  adsorbs in a cationic form as  $R_1C(OH)^+R_2^*(g)$  (step T7). To conclude the thermochemical cycle,  $R_1C(OH)^+R_2^*(g)$ ,  $H^*(g)$ , and the Ru surface (with  $e^-_{\text{band}}$ ) are solvated by the solvent and their solvation effects are treated here with a dielectric continuum ( $\epsilon_r > 1$ , step T8).

Since the Gibbs free energy change from step T1 to step T8 ( $\Delta G_{T1-T8}$ , Scheme 4) equals that from step 1 to step 4 ( $\Delta G_{1-4}$ , Scheme 3):

$$\Delta G_{T1-T8} = \Delta G_{1-4} \quad (19)$$

Section S8 in the Supporting Information provides the derivation of the energies used in the following discussion. The free energies related to the desolvation of  $R_1C(O)R_2(g)$  (in  $\Delta G_{T1}$ ) for all aliphatic carbonyls in the same homologous series are essentially constant for a given solvation environment (e.g.,  $-15 \pm 1 \text{ kJ mol}^{-1}$  for  $R_1C(O)R_2(g)$  aqueous phase solvation free energy<sup>27</sup>). Similarly, free energy changes for the solvation of  $R_1C(OH)^+R_2^*(g)$ ,  $H^*(g)$ , and the Ru surface (with  $e^-_{\text{band}}$ ) ( $\Delta G_{T8}$ ) also remain the same for all aliphatic carbonyls (Sections S3 and S7). Note that the solvation free energies of aromatic carbonyls and of their charged hydroxy intermediates deviate from those of their aliphatic counterparts. This difference in solvation free energy potentially contributes to the higher hydrogenation reactivity of acetophenone in comparison to the predicted trend derived from aliphatic ketones (Figure 4b). The terms  $\Delta G_{T2}$ ,  $\Delta G_{T3}$ ,  $\Delta G_{T5}$ , and  $\Delta G_{T6}$ , which refer to the changes in free energies during  $H_2(g)$  dissociation, H-radical ionization, electron transfer, and H-radical adsorption, respectively, are unrelated to carbonyl or solvent identities; thus, their values must remain constant, when the rate data in Figures 1 and 4 are interpreted. The  $R_1C(OH)^+R_2(g)$  adsorption free energies ( $\Delta G_{T7}$ ), estimated from the enthalpies of  $R_1C(OH)R_2^*(g)$  adsorption (Sections S3 and S7), are relatively constant across the various aliphatic carbonyl species (e.g.,  $\pm 7 \text{ kJ mol}^{-1}$  on Ru(0001)).<sup>1a</sup> Protonated acetophenone,  $ArC(OH)^+CH_3(g)$ , may adsorb much more strongly on Ru surfaces due to its additional aromaticity, leading  $\Delta G_{T7}$  to be more negative and thus the rates to become higher than the predicted value from aliphatic ketones (Figure 4b). Therefore, the variation of  $\Delta G_{1-4}$  (eq 19) reflects predominantly the change in the protonation free energies of the aliphatic carbonyls ( $\Delta G_{T4}$ ). The gas-phase proton affinity of  $R_1C(O)R_2(g)$  varies from 786 to 827  $\text{kJ mol}^{-1}$ ,<sup>14</sup> whereas the protonation entropy ranges from 2 to 9  $\text{J mol}^{-1} \text{ K}^{-1}$ ,<sup>14</sup> the latter translates to a free energy change of  $< 3 \text{ kJ mol}^{-1}$  at 323 K. When these small entropic contributions are ignored ( $\Delta G_{T4} = -PA_{R_1C(O)R_2(g)} - T\Delta S_{T4} \approx -PA_{R_1C(O)R_2(g)}$ , because  $T\Delta S_{T4} < 0.4\%$  of  $\Delta G_{T4}$ , Section S4 in the Supporting Information), eq 18 becomes (derivation in Section S8)

$$\Delta_{\text{reactant}}[k_{R_1C(O)R_2,M,H_2O}^{1st}] = \chi_M \Delta_{\text{reactant}} \left[ \exp \left( \frac{PA_{R_1C(O)R_2(g)}}{RT} \right) \right] \quad (20a)$$

where

$$\chi_M \approx k_{sa} P_{H_2} \theta_*^2 \exp \left( \frac{-\sum_{x=1}^3 \Delta G_{Tx} - \sum_{x=5}^5 \Delta G_{Tx}}{RT} \right) \quad (20b)$$

Equation 20a predicts that  $k_{R_1C(O)R_2,M,H_2O}^{1st}$  increases exponentially with increasing gas-phase proton affinity of the carbonyls ( $PA_{R_1C(O)R_2(g)}$ ), consistent with the first-order rate coefficient

and lumped rate constant trends in Figures 1a and 4 and with the PET pathway as the predominant hydrogenation route.

The parameter  $\chi_M$  (eqs 20a and 20b) captures the metal identity effects on hydrogenation rates (Figure 1a). The change in metal identity not only modifies the parameters in the thermochemical construct (i.e.,  $\Delta G_{Ts}$ , approximated by a negative value of the metal work function ( $WF_M$ ),<sup>5a,23c</sup>  $\Delta G_{T6}$ , and  $\Delta G_{T7}$ , in Scheme 4) but also affects the intrinsic rate constant ( $k_{sa}$ ) and vacant site density ( $\theta_*$ ) during catalysis among the different metal surfaces. Interpreting the periodic trends across the different metals in Figure 1a thus requires further, comprehensive rate assessments decoupling the intrinsic rate constants and surface coverages from each other.

The Born–Haber thermochemical cycle captures the solvent identity effects shown in Figure 1b. Since the free energy changes between step T2 and step T7 reflect solely the gas-phase properties, their values do not vary with the solvent identity. In contrast, the solvation free energies ( $\Delta G_{T1}$  and  $\Delta G_{T8}$ ), which represent the free energy differences between steps 1 and 4 (eqs 18 and 19), vary with the solvent identity. We project the solvent as a dielectric continuum and estimate the solvation free energies for charged and noncharged species on the basis of the Born equation<sup>15</sup> and Kirkwood formula,<sup>28</sup> respectively. Due to the insignificant dipole moment  $H^*(g)$ ,<sup>23c,29</sup> the solvation free energies of  $H^*(g)$  are negligible. The solvation free energy change of  $C_2H_5C(O)CH_3(g)$  is insignificant throughout the examined solvation environment ( $< 0.5 \text{ kJ mol}^{-1}$ , Section S9 in the Supporting Information). Since all R'OH solvents have comparable heats of adsorption ( $\sim 30 \pm 10 \text{ kJ mol}^{-1}$ ,<sup>23b</sup>), the vacant site densities  $\theta_*$  do not vary significantly across the different solvents, and eq 18 simplifies to

$$\Delta_{\text{solvent}}[k_{C_2H_5C(O)CH_3,Ru,1}^{1st}] = \gamma \Delta_{\text{solvent}} \left[ \exp \left( \frac{\sigma(1 - \epsilon_r^{-1})}{RT} \right) \right] \quad (21a)$$

where

$$\sigma = \frac{q^2 N_A}{8\pi \epsilon_0 R_{C_2H_5C(OH)^+CH_3^*(g)}} \quad (21b)$$

and

$$\gamma = k_{sa} P_{H_2} \theta_*^2 \exp \left( -\frac{\Delta G_{\text{sol},C_2H_5C(O)CH_3(g)} + \sum_{x=2}^7 \Delta G_{Tx}}{RT} \right) \quad (21c)$$

and  $q$ ,  $N_A$ ,  $\epsilon_0$ ,  $R_{C_2H_5C(OH)^+CH_3^*(g)}$ , and  $\Delta G_{\text{sol},C_2H_5C(O)CH_3(g)}$  denote the elementary electron charge, Avogadro's constant, the permittivity of free space, the radius of  $C_2H_5C(OH)^+CH_3^*(g)$ , and the solvation free energy of  $C_2H_5C(O)CH_3(g)$ , respectively. Equation 21a predicts that  $k_{C_2H_5C(O)CH_3,Ru,1}^{1st}$  decreases exponentially when the inverse of the solvent dielectric permittivity ( $\epsilon_r^{-1}$ ) increases, consistent with the experimental observations in Figure 1b.

In summary, thermochemical analyses via the Born–Haber construct in Scheme 4 illustrate the origin of the observed reactivity trends with the chemical identity of reactant and solvent. The analyses also directly pinpoint the reactants' proton affinity and solvents' dielectric permittivity as the kinetic descriptors.

## 4. CONCLUSIONS

We report kinetic and isotopic evidence for the involvement of proton–electron transfer events during condensed-phase hydrogenation of aldehydes and ketones on Ru clusters, when polar protic solvents are used. In the presence of protic solvent molecules, hydrogenation occurs via an initial ionization of a hydrogen adatom followed by the transfer of a proton onto its carbonyl oxygen atom, before the sequential, kinetically relevant hydrogen adatom transfer onto the carbonyl carbon. Kinetic and thermodynamic analyses show that both proton affinities of the carbonyl reactant ( $PA_{R_1C(O)R_2(g)}$ ) and dielectric permittivities of the solvent ( $\epsilon_r$ ) influence the stabilities of the ionic O–H bond formed in charged hydroxy intermediates ( $R_1C(OH)^+R_2^*$ ) as a result of the proton transfer. As  $PA_{R_1C(O)R_2(g)}$  increases or as  $\epsilon_r^{-1}$  decreases, the charged hydroxy intermediates become preferentially stabilized and popularized on metal surfaces. Such stabilizations of the intermediates also lower the free energies of the transition state of the sequential, kinetically relevant hydrogen addition step that adds a hydrogen adatom to the carbonyl carbon and in turn lead to an exponential increase in the overall hydrogenation rates. A Born–Haber thermochemical cycle decomposes the free energy for the formation of charged hydroxy intermediate into measurable, predictable energetics. The analysis confirms that the proton affinities of the carbonyl reactant ( $PA_{R_1C(O)R_2(g)}$ ) and dielectric permittivities of the solvent ( $\epsilon_r$ ) directly influence the stability of the charged hydroxy intermediate at protic solvent and transition-metal interfaces and thus are the kinetic descriptors of the reaction. This work offers experimental evidence of proton–electron transfer during the hydrogenation of carbonyls at the protic solvent–transition metal interfaces and rationalizes the reactivity trends through a mechanistic framework, completed with free energy analyses and their decomposition into measurable thermochemical properties.

## ■ ASSOCIATED CONTENT

### Supporting Information

The Supporting Information is available free of charge on the ACS Publications website at DOI: 10.1021/acscatal.8b03470.

Additional derivation information (PDF)

## ■ AUTHOR INFORMATION

### Corresponding Author

\*Y.-H.C.C.: e-mail, [cathy.chin@utoronto.ca](mailto:cathy.chin@utoronto.ca); tel, (416) 978-8868; fax, (416) 978-8605.

### ORCID

Ya-Huei Cathy Chin: 0000-0003-4388-0389

### Notes

The authors declare no competing financial interest.

## ■ ACKNOWLEDGMENTS

This study was supported by the Natural Sciences and Engineering Research Council of Canada (NSERC) and Ontario Centres of Excellence. We acknowledge Dr. Joachim Ritter (Dupont) for helpful technical discussions, Zhenwei Wu for the measurement of exchange to hydrogenation rate ratio via *Alkoxy* pathway in the gas phase, and Gabriel Negrelli Garcia for his contribution on the development stage of the experimental work. J.S. acknowledges a Hatch Graduate Scholarship for Sustainable Energy Research for support.

## ■ REFERENCES

- (1) (a) Sinha, N. K.; Neurock, M. A first principles analysis of the hydrogenation of C 1 C 4 aldehydes and ketones over Ru (0001). *J. Catal.* **2012**, *295*, 31–44. (b) Loveless, B. T.; Buda, C.; Neurock, M.; Iglesia, E. CO Chemisorption and Dissociation at High Coverages during CO Hydrogenation on Ru Catalysts. *J. Am. Chem. Soc.* **2013**, *135*, 6107–6121. (c) Horiuti, I.; Polanyi, M. Exchange reactions of hydrogen on metallic catalysts. *Trans. Faraday Soc.* **1934**, *30*, 1164–1172.
- (2) (a) Hibbitts, D. D.; Loveless, B. T.; Neurock, M.; Iglesia, E. Mechanistic Role of Water on the Rate and Selectivity of Fischer–Tropsch Synthesis on Ruthenium Catalysts. *Angew. Chem., Int. Ed.* **2013**, *52*, 12273–12278. (b) Wilson, N. M.; Flaherty, D. W. Mechanism for the Direct Synthesis of H<sub>2</sub>O<sub>2</sub> on Pd Clusters: Heterolytic Reaction Pathways at the Liquid–Solid Interface. *J. Am. Chem. Soc.* **2016**, *138*, 574–586. (c) Wilson, N. M.; Pan, Y.-T.; Shao, Y.-T.; Zuo, J.-M.; Yang, H.; Flaherty, D. W. Direct Synthesis of H<sub>2</sub>O<sub>2</sub> on AgPt Octahedra: The Importance of Ag–Pt Coordination for High H<sub>2</sub>O<sub>2</sub> Selectivity. *ACS Catal.* **2018**, *8*, 2880–2889.
- (3) Skúlason, E.; Karlberg, G. S.; Rossmeisl, J.; Bligaard, T.; Greeley, J.; Jónsson, H.; Nørskov, J. K. Density functional theory calculations for the hydrogen evolution reaction in an electrochemical double layer on the Pt (111) electrode. *Phys. Chem. Chem. Phys.* **2007**, *9*, 3241–3250.
- (4) Trasatti, S. Work function, electronegativity, and electrochemical behaviour of metals: III. Electrolytic hydrogen evolution in acid solutions. *J. Electroanal. Chem. Interfacial Electrochem.* **1972**, *39*, 163–184.
- (5) (a) Wagner, F. T.; Moylan, T. E. Generation of surface hydronium from water and hydrogen coadsorbed on Pt (111). *Surf. Sci.* **1988**, *206*, 187–202. (b) Kim, Y.; Shin, S.; Kang, H. Zundel-like and Eigen-like Hydrated Protons on a Platinum Surface. *Angew. Chem., Int. Ed.* **2015**, *54*, 7626–7630.
- (6) Pan, M.; Pozun, Z. D.; Yu, W.-Y.; Henkelman, G.; Mullins, C. B. Structure revealing H/D exchange with co-adsorbed hydrogen and water on gold. *J. Phys. Chem. Lett.* **2012**, *3*, 1894–1899.
- (7) Lackey, D.; Schott, J.; Sass, J.; Woo, S.; Wagner, F. Surface-science simulation study of the electrochemical charge-transfer reaction (H) ad + (H 2 O) ad → (H 3 O+) ad + e− metal on Pt (111) and Cu (110). *Chem. Phys. Lett.* **1991**, *184*, 277–281.
- (8) Paredes Olivera, P.; Ferral, A.; Patrito, E. Theoretical investigation of hydrated hydronium ions on Ag (111). *J. Phys. Chem. B* **2001**, *105*, 7227–7238.
- (9) Desai, S. K.; Neurock, M. First-principles study of the role of solvent in the dissociation of water over a Pt–Ru alloy. *Phys. Rev. B: Condens. Matter Mater. Phys.* **2003**, *68*, 075420.
- (10) (a) Tuckerman, M.; Laasonen, K.; Sprik, M.; Parrinello, M. Abinitio molecular dynamics simulation of the solvation and transport of hydronium and hydroxyl ions in water. *J. Chem. Phys.* **1995**, *103*, 150–161. (b) Marx, D.; Tuckerman, M. E.; Hutter, J.; Parrinello, M. The nature of the hydrated excess proton in water. *Nature* **1999**, *397*, 601–604. (c) Tuckerman, M. E.; Marx, D.; Parrinello, M. The nature and transport mechanism of hydrated hydroxide ions in aqueous solution. *Nature* **2002**, *417*, 925–929.
- (11) (a) Huynh, M. H. V.; Meyer, T. J. Proton-Coupled Electron Transfer. *Chem. Rev.* **2007**, *107*, 5004–5064. (b) Sirjoosingh, A.; Hammes-Schiffer, S. Proton-Coupled Electron Transfer versus Hydrogen Atom Transfer: Generation of Charge-Localized Diabatic States. *J. Phys. Chem. A* **2011**, *115*, 2367–2377. (c) Warren, J. J.; Tronic, T. A.; Mayer, J. M. Thermochemistry of proton-coupled electron transfer reagents and its implications. *Chem. Rev.* **2010**, *110*, 6961–7001.
- (12) (a) Akpa, B. S.; D’Agostino, C.; Gladden, L. F.; Hindle, K.; Manyar, H.; McGregor, J.; Li, R.; Neurock, M.; Sinha, N.; Stitt, E. H.; Weber, D.; Zeitler, J. A.; Rooney, D. W. Solvent effects in the hydrogenation of 2-butanone. *J. Catal.* **2012**, *289*, 30–41. (b) Wan, H.; Vitter, A.; Chaudhari, R. V.; Subramaniam, B. Kinetic investigations of unusual solvent effects during Ru/C catalyzed hydrogenation of model oxygenates. *J. Catal.* **2014**, *309*, 174–184. (c) Shangguan, J.; Olarte, M. V.; Chin, Y.-H. Mechanistic insights on CO and CC bond activation

and hydrogen insertion during acetic acid hydrogenation catalyzed by ruthenium clusters in aqueous medium. *J. Catal.* **2016**, *340*, 107–121.

(13) Ertl, G.; Knözinger, H.; Schüth, F.; Weitkamp, J. *Handbook of heterogeneous catalysis: 8 volumes*. Wiley-VCH: 2008; p 741.

(14) Hunter, E. P.; Lias, S. G. Evaluated gas phase basicities and proton affinities of molecules: an update. *J. Phys. Chem. Ref. Data* **1998**, *27*, 413–656.

(15) Atkins, P. *Physical Chemistry*, 6th ed.; Oxford University Press: 1998; p 110.

(16) Wauquier, J. P.; Jungers, J. C. La Cinétique Quantitative En Catalyse Hétérogène-L'influence Du Milieu Sur L'activité Et La Sélectivité Du Catalyseur. *Bull. Soc. Chim. France* **1957**, *8-9*, 1280–1288.

(17) (a) Wan, H.; Vitter, A.; Chaudhari, R. V.; Subramaniam, B. Kinetic investigations of unusual solvent effects during Ru/C catalyzed hydrogenation of model oxygenates. *J. Catal.* **2014**, *309*, 174–184.

(b) Abdelrahman, O. A.; Heyden, A.; Bond, J. Q. Microkinetic analysis of C 3–C 5 ketone hydrogenation over supported Ru catalysts. *J. Catal.* **2017**, *348*, 59–74.

(18) Kellner, C. S.; Bell, A. T. Evidence for H<sub>2</sub>D<sub>2</sub> isotope effects on Fischer-Tropsch synthesis over supported ruthenium catalysts. *J. Catal.* **1981**, *67*, 175–185.

(19) Chase, M. W., Jr.; Tables, N.-J. T. Data reported in NIST standard reference database 69, June 2005 release: NIST Chemistry WebBook. *J. Phys. Chem. Ref. Data, Monograph* **1998**, *9*, 1–1951.

(20) Luo, Y.-R. *Comprehensive handbook of chemical bond energies*; CRC Press: 2007; p 19.

(21) Ojeda, M.; Li, A.; Nabar, R.; Nilekar, A. U.; Mavrikakis, M.; Iglesia, E. Kinetically Relevant Steps and H<sub>2</sub>/D<sub>2</sub> Isotope Effects in Fischer-Tropsch Synthesis on Fe and Co Catalysts. *J. Phys. Chem. C* **2010**, *114*, 19761–19770.

(22) (a) Westheimer, F. The magnitude of the primary kinetic isotope effect for compounds of hydrogen and deuterium. *Chem. Rev.* **1961**, *61*, 265–273. (b) Klinman, J. P., Primary hydrogen isotope effects. In *Transition states of Biochemical Processes*; Springer: 1978; pp 165–200.

(23) (a) Feibelman, P. J. Partial Dissociation of Water on Ru(0001). *Science* **2002**, *295*, 99–102. (b) Michaelides, A.; Alavi, A.; King, D. A. Different Surface Chemistries of Water on Ru{0001}: From Monomer Adsorption to Partially Dissociated Bilayers. *J. Am. Chem. Soc.* **2003**, *125*, 2746–2755. (c) Santen, R. A. V.; Neurock, M. *Molecular heterogeneous catalysis*; Wiley-VCH: 2006; p 474.

(24) (a) Eigen, M. Proton Transfer, Acid-Base Catalysis, and Enzymatic Hydrolysis. Part I: ELEMENTARY PROCESSES. *Angew. Chem., Int. Ed. Engl.* **1964**, *3*, 1–19. (b) Bell, R. P. *The proton in chemistry*; Springer Science & Business Media: 2013; p 194. (c) Caldin, E. *The mechanisms of fast reactions in solution*; Ios Press: 2001; p 7.

(25) Wiberg, K. B. The deuterium isotope effect. *Chem. Rev.* **1955**, *55*, 713–743.

(26) Scheiner, S.; Čuma, M. Relative stability of hydrogen and deuterium bonds. *J. Am. Chem. Soc.* **1996**, *118*, 1511–1521.

(27) Sitkoff, D.; Sharp, K. A.; Honig, B. Accurate Calculation of Hydration Free Energies Using Macroscopic Solvent Models. *J. Phys. Chem.* **1994**, *98*, 1978–1988.

(28) (a) Kirkwood, J. G. Theory of Solutions of Molecules Containing Widely Separated Charges with Special Application to Zwitterions. *J. Chem. Phys.* **1934**, *2*, 351–361. (b) Kirkwood, J. G.; Westheimer, F. H. The Electrostatic Influence of Substituents on the Dissociation Constants of Organic Acids. I. *J. Chem. Phys.* **1938**, *6*, 506–512. (c) Reichardt, C.; Welton, T. *Solvents and solvent effects in organic chemistry*; Wiley: 2011; p 87.

(29) Iyemperumal, S. K.; Deskins, N. A. Evaluating Solvent Effects at the Aqueous/Pt (111) Interface. *ChemPhysChem* **2017**, *18*, 2171–2190.

(30) Wohlfarth, C. *Static dielectric constants of pure liquids and binary liquid mixtures: supplement to IV/6*; Springer Science & Business Media: 2008; pp 4–495.

(31) Åkerlöf, G.; Short, O. A. The dielectric constant of dioxane—water mixtures between 0 and 80. *J. Am. Chem. Soc.* **1936**, *58*, 1241–1243.